

UNCLASSIFIED

AD NUMBER

ADB001025

LIMITATION CHANGES

TO:

Approved for public release; distribution is unlimited.

FROM:

Distribution authorized to U.S. Gov't. agencies only; Test and Evaluation; . Other requests shall be referred to Air Force Armament Laboratory (DLYV), Eglin Air Force Base, FL 32542.

AUTHORITY

AFATL ltr, 2 feb 1977

THIS PAGE IS UNCLASSIFIED

THIS REPORT HAS BEEN DELIMITED
AND CLEARED FOR PUBLIC RELEASE
UNDER DOD DIRECTIVE 5200.20 AND
NO RESTRICTIONS ARE IMPOSED UPON
ITS USE AND DISCLOSURE.

DISTRIBUTION STATEMENT A

APPROVED FOR PUBLIC RELEASE;
DISTRIBUTION UNLIMITED.

ADB001025

AFATL-TR-74-120

**DYNAMIC RESPONSE OF STRUCTURES
AND MATERIALS TO IMPULSIVE LOADS**

**DEPARTMENT OF ENGINEERING SCIENCES
UNIVERSITY OF FLORIDA
GAINESVILLE, FLORIDA 32611**

JULY 1974

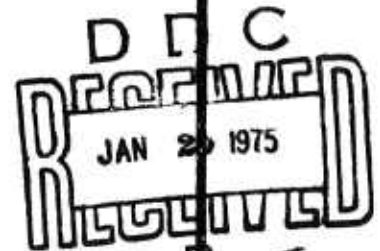
**FINAL REPORT
FOR PERIOD 19 OCTOBER 1973 - 30 JUNE 1974**

Distribution limited to U. S. Government agencies only;
this report documents test and evaluation; distribution
limitation applied July 1974 . Other requests for
this document must be referred to the Air Force Armament
Laboratory (DLYV), Eglin Air Force Base, Florida 32542.

AIR FORCE ARMAMENT LABORATORY

AIR FORCE SYSTEMS COMMAND • UNITED STATES AIR FORCE

EGLIN AIR FORCE BASE, FLORIDA



UNCLASSIFIED

SECURITY CLASSIFICATION OF THIS PAGE (When Data Entered)

| REPORT DOCUMENTATION PAGE | | READ INSTRUCTIONS BEFORE COMPLETING FORM |
|--|-----------------------|---|
| 1. REPORT NUMBER AFATL-TR-74-120 | 2. GOVT ACCESSION NO. | 3. RECIPIENT'S CATALOG NUMBER |
| 4. TITLE (and Subtitle) DYNAMIC RESPONSE OF STRUCTURES AND MATERIALS TO IMPULSIVE LOADS | | 5. TYPE OF REPORT & PERIOD COVERED 19 Oct 1973 - 30 Jun 1974 |
| 7. AUTHOR(s) C. Allen Ross Robert L. Sierakowski Lawrence E. Malvern | | 6. PERFORMING ORG. REPORT NUMBER |
| 9. PERFORMING ORGANIZATION NAME AND ADDRESS Department of Engineering Sciences University of Florida Gainesville, Florida 32611 | | 8. CONTRACT OR GRANT NUMBER(s) F08635-74-C-0036 |
| 11. CONTROLLING OFFICE NAME AND ADDRESS Air Force Armament Laboratory Air Force Systems Command Eglin Air Force Base, FL 32542 | | 10. PROGRAM ELEMENT, PROJECT, TASK AREA & WORK UNIT NUMBERS Project No. 2549 Task No. 02 Work Unit No. 14 |
| 14. MONITORING AGENCY NAME & ADDRESS (if different from Controlling Office) | | 12. REPORT DATE July 31, 1974 |
| | | 13. NUMBER OF PAGES 93 |
| | | 15. SECURITY CLASS. (of this report) UNCLASSIFIED |
| | | 15a. DECLASSIFICATION DOWNGRADING SCHEDULE |
| 16. DISTRIBUTION STATEMENT (of this Report) Distribution limited to U. S. Government agencies only; this re- port documents test and evaluation; distribution limitation applied July 1974. Other requests for this document must be referred to the Air Force Armament Laboratory (DLTV), Eglin Air Force Base, Florida 32542. | | |
| 17. DISTRIBUTION STATEMENT (of the abstract entered in Block 20, if different from Report) | | |
| 18. SUPPLEMENTARY NOTES Available in DDC. | | |
| 19. KEY WORDS (Continue on reverse side if necessary and identify by block number) Impulsive loading Fuel-Air Explosion Concrete Beams Cratering Wave propagation Plastic hinge Dynamic response Contact explosion | | |
| 20. ABSTRACT (Continue on reverse side if necessary and identify by block number) This report is divided into three main subjects, e. g., beam re- sponse to impulsive loads of fuel-air explosions (FAE), effect of fuel-air explosions in confined unpressurized containers, and the effect of intense impulsive loads from surface blasts on material removal and degradation of a concrete semi-half space. Investiga- tion into the response of small ductile beam elements subjected to blast loadings indicates a need for analysis of beams including | | |

DD FORM 1473

1 JAN 73

EDITION OF 1 NOV 65 IS OBSOLETE

UNCLASSIFIED

SECURITY CLASSIFICATION OF THIS PAGE (When Data Entered)

UNCLASSIFIED

SECURITY CLASSIFICATION OF THIS PAGE(When Data Entered)

20. Abstract Continued

gross deformation, axial constraints, and complete failure. The response of small beams to fuel-air explosions fall in a transition between a static mechanism and a traveling plastic hinge mechanism. Equations of motion, based on a strength of material approach, are derived for both mechanisms. The same general shock transmission and reflection of detonation waves are found to be operative in both confined and unconfined fuel-air explosions. The ratio of the reflected pressure to the static pressure of a detonation wave is dependent only on the ratio of specific heats and reaches a maximum of 2.6 for a specific heat ratio of infinity. Computational models are available and have been used with some success for prediction of cratering, material removal and material degradation for certain rock media and could be used for concrete; however, development of constitutive models for concrete is still in the fundamental stage. More fundamental research, especially experimental and theoretical work on material characterization, is needed before a reasonable damage estimation of concrete subjected to intense impulsive loads can be obtained.

UNCLASSIFIED

SECURITY CLASSIFICATION OF THIS PAGE(When Data Entered)

PREFACE

This report represents the results of a study of dynamic response of simple structural elements and semi-infinite materials to impulsive loads. This study was conducted during the period from 19 October 1973 through 30 June 1974, by the Department of Engineering Sciences, University of Florida, Gainesville, Florida, under Contract No. F08635-74-C-0036 with the Air Force Armament Laboratory, Eglin Air Force Base, Florida. Mr. W. Stanley Strickland (DLYV) served as program manager for the Armament Laboratory.

This technical report has been reviewed and approved for publication.

FOR THE COMMANDER



ROY C. COMPTON
Chief, Weapon Systems Analysis Division

TABLE OF CONTENTS

| Section | Title | Page |
|------------|---|------|
| I | Failure of Simple Structural Elements Subjected to Impulsive Loads | 9 |
| II | Fuel-Air Explosion (FAE) in Confined Structures | 35 |
| III | Structural Degradation of Concrete by Impulsive Loads | 39 |
| Appendix | Literature Search, Laboratory Visits, Technical Meetings | 81 |
| References | | 84 |

LIST OF FIGURES

| Figure | Title | Page |
|--------|---|------|
| 1 | Schematic of Plate Response Mechanisms | 10 |
| 2 | Idealized Stress-Strain Curve | 13 |
| 3 | Bending Stress Distribution | 13 |
| 4 | Static Beam Failure Due to Plastic Hinge | 15 |
| 5 | Moving Plastic Hinge Mechanism | 16 |
| 6 | Typical Blast Pressure Time Curve for a Fuel-Air Explosion | 17 |
| 7 | Traveling Plastic Hinge Mechanism and Free Body Diagram | 19 |
| 8 | Beam Response Mechanism Including Axial Constraint | 21 |
| 9 | Impulse Required for Shear Failure Mode of Beams | 24 |
| 10 | Free Body Diagram for a Static Analysis of a Beam Fixed at Both Ends | 25 |
| 11 | Schematic of Plastic Zone | 29 |
| 12 | Schematic of Traveling Plastic Hinge Mechanism | 30 |
| 13 | Pressure of a Fuel-Air Explosion Versus Distance from the Secondary Explosion | 38 |
| 14 | Typical Half-Crater Profile from a Surface or Near-Surface Shot Over a Hard Rock Medium | 40 |
| 15 | True Crater Dimensions as a Function of Charge Weight for True Surface (Dashed Curves) and $0.9r_c HOB$ (Solid Curves) Shot Geometries | 48 |

LIST OF FIGURES (Concluded)

| Figure | Title | Page |
|--------|--|------|
| 16 | Comparison of Scaling True Crater Depth by $W^{1/2.7}$ as Opposed by Scaling by Charge Radii ($W^{1/3}$ Scaling) with a constant $W^{1/3}$ Scaling Factor for Height of Burst | 52 |
| 17 | True Crater Radius, Scaled by $W^{1/2.7}$, as a Function of Height (or Depth) of Burst, Scaled by $W^{1/3}$ (Geometric Scaling) for Spherical TNT Charges Fired in Hard Rock . . . | 53 |
| 18 | Experimental Configuration for Measuring Spherical Stress Wave Response at Different Radii | 58 |
| 19 | Experimental Radial Stress-Time Histories for Spherical Waves in Various Geological Materials | 59 |
| 20 | Experimental Particle Velocity-Time Histories in PI MIXED COMPANY Dry Sandstone. . | 60 |
| 21 | Top and Side View of Concrete Block Assembly. Gage Geometry in this Drawing Corresponds To Experiment 11-A of Reference 55 | 61 |
| 22 | Stress or Particle Velocity Histories from Multiple Gages are Combined to Form a Surface in the Space-Time Plane | 68 |
| 23 | Typical Specimens for Static Tests | 73 |
| 24 | Dynamic Impact Bar Specimens | 74 |
| 25 | Dynamic Impact Test Assembly | 75 |
| 26 | Typical Dynamic Tensile Fractures | 75 |
| 27 | Typical Strain Profiles for Impacted Concrete Bars | 76 |

LIST OF TABLES

| Table | Title | Page |
|-------|---|------|
| 1 | Beam Shape Factor | 14 |
| 2 | Beam Response to Impulsive Loads | 31 |
| 3 | Properties of Cement Grout | 50 |
| 4 | True Crater Dimensions | 51 |
| 5 | Specimen Composition | 72 |
| 6 | Average Static Properties | 72 |
| 7 | Dynamic Tensile Fracture | 78 |
| A-1 | List of Literature Searches | 81 |
| A-2 | Places and Laboratories Visited and Conferences Attended | 82 |
| A-3 | Categories of Abstracts from Literature Search | 82 |

LIST OF SYMBOLS

| | |
|---------------------------------|--|
| A | beam cross section area (in ²) |
| C | stress wave velocity (in/sec) |
| C _u | aggregate uniformity ratio |
| c | maximum fiber distance of beam (in) |
| D | detonation wave velocity (in/sec) |
| D ₅₀ | seive size passing 50% of sample |
| d | crater depth (in) |
| f | beam shape factor |
| G | shear modulus (psi) |
| HOB | height of burst (in) |
| h | beam thickness (in) |
| h | general Lagrangian radius (in) |
| I, I(t) | impulse-time function (psi-msec) |
| I | impulse per unit length (psi-msec/in) |
| J | total impulse (lb-sec) |
| J ₁ , J ₂ | stress invariant (psi) |
| K | bulk modulus (psi) |
| KE | kinetic energy (in-lb) |
| L | beam half span (in) |
| L | Lagrangian function $L = KE - PE$ (in-lb) |
| L _p | plastic zone length (in) |
| M _p | plastic moment (in-lb) |
| M _y | yield moment (in-lb) |

LIST OF SYMBOLS (Continued)

| | |
|--------------------------------|--|
| m | mass per unit length (lb-sec ² /in ⁵) |
| N | force per unit length (lb/in) |
| n_1, n_2, n_3 | superscript for explosive weight |
| PE | plastic strain energy (in-lb) |
| p,p(t) | pressure time function (psi) |
| P _o ,P _s | static collapse pressure (psi) |
| P _r | reflected pressure (psi) |
| Q | generalized force (lb) |
| R | radius of beam curvature (in) |
| r | general variable radius (in) |
| S | planar moment of inertia (in ⁴) |
| S _{ij} | stress deviator |
| t | time (sec) |
| u | displacement (in) |
| V, V _o | beam centerpoint velocity (in/sec) |
| \bar{V} | crater volume (in ³) |
| W | explosive weight (lb) |
| w | beam width (in) |
| x,y | beam coordinates (in) |
| x _h | plastic hinge position (in) |
| y _f | beam centerpoint deflection (in) |
| z | beam section modulus (in ³) |

LIST OF SYMBOLS (Concluded)

| | |
|-----------------|---|
| γ | ratio of specific heats |
| Δ | longitudinal beam deflection (in) |
| δ | beam midspan deflection (in) |
| ϵ | strain (in/in) |
| ϵ_{ij} | strain deviator (psi) |
| ϵ_{kk} | dilatation (in/in) |
| θ | beam rotation (rad) |
| ρ | mass density (lb-sec ² /in ⁴) |
| σ_r | radial stress (psi) |
| σ_y | yield stress (psi) |
| σ_θ | tangential stress (psi) |
| τ | length of blast positive pressure phase (sec) |
| ϕ | stress difference $\phi = \sigma_r - \sigma_\theta$ (psi) |
| ω | beam angular velocity (rad/sec) |

SECTION I

FAILURE OF SIMPLE STRUCTURAL ELEMENTS SUBJECTED TO IMPULSIVE LOADS

1.1 Introduction

Failure of a structural element may be defined in many ways thus giving a very wide range of choices for definition of failure. A structural element may be considered as having failed after having exceeded some load or stress level, some local distortion or some large deflection due to a buckling phenomena. To further complicate a failure definition various kinds of loads may produce the stress level or distortion necessary for failure. Failure of a structural element is therefore a very broad term and a given definition must be quite specific when describing failure. For this discussion failure shall be defined as a condition when actual rupture, fracture, or breakage occurs at some point in the material and renders the structural element incapable of resisting any further loading. This discussion shall be restricted to failure of very basic elements such as beams, plates, rods, etc., and will not be concerned with failure of a large or complicated structure comprising many of the basic elements.

A response mechanism of a structural element may be defined as the general shape or manner of deformation leading to the final deformed state of the element. Plate and beam response associated with blast loading are usually one of two types, (1) a static mechanism where the initial deflection shape is continued on through failure, or (2) a traveling plastic hinge mechanism which changes the deflected shape continuously for some stage of the deformation process. The response mechanism taken on by a structural element is not only dependent on the general properties of the structure but is also strongly dependent on the magnitude of the peak overpressure and duration of the blast or impulsive loading.

A failure mode may then be defined in a manner associated with the loading placed on the structure by the response mechanism. If the response mechanism is such as to place the member in tension until failure, then this would be called a tension failure mode. Combinations of response mechanisms may exist and combined failure modes may occur under combined stresses or strains.

In order that a failure load may be predicted, it is necessary to know both the mechanism and mode of failure. The response mechanism determines the irreversible path taken by the structural element and the energy required or work done in moving the element through that path may be predicted quite readily. Using the failure mode based on knowledge gained from the response mechanism a failure criteria based on a maximum stress or deformation may be applied for that particular failure mode. Since complete failure of structural elements is rather complicated it is best that a discussion of the entire assumed failure process and resulting analysis be given under one general heading entitled plates, beams, etc. In this light the remainder of this section will be devoted to a discussion of plates and beams subjected to impulsive loads.

1.2 Flat Plates

The response of flat plates when subjected to impulsive loads resulting from blast loadings, as mentioned previously, is usually divided into two types of mechanisms: (1) the static case where the plate deforms in some continuous uniform shape as shown in Figure 1a, and (2) a plastic hinge case where the initial deflection is by propagation of stress wave or plastic hinges as shown in Figure 1b. For plates with high short side

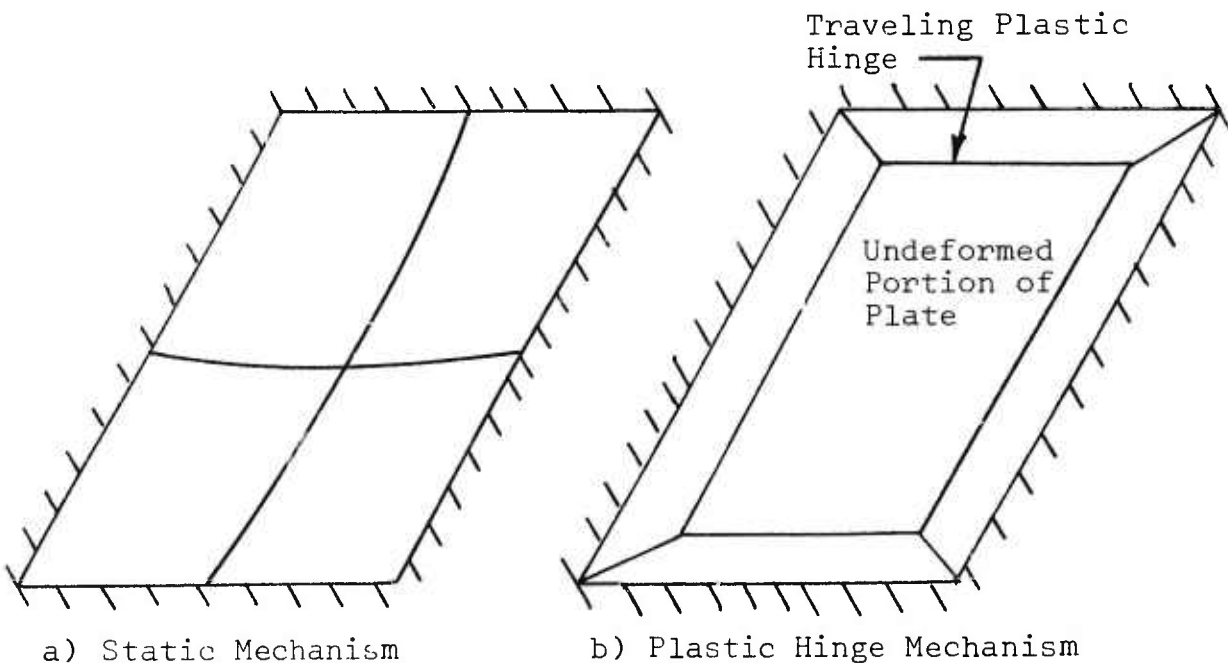


Figure 1. Schematic of Plate Response Mechanisms

dimension to thickness ratios, where bending is negligible compared to the membrane forces, the resultant failure mode for the static mechanism is tension. The location of the failure is dependent on the plate boundary conditions and distribution of load. The plastic hinge mechanism operating in the same plate is characterized by a tensile stress wave (plastic hinge) originating at the boundaries and moving toward the center of the plate. The failure mode is one of tension which may occur near the edges of the plate in the early stage of plate deformation or at other positions in the plate where high strains result from the initial transmission and/or reflections of the stress wave. Generally, the dividing region governing which mechanism occurs is defined in terms of the characteristic period of the elastic plate frequency and the positive phase of the pressure pulse. If the positive pressure phase of the pressure pulse is greater than one-quarter of the characteristic period of the plate, then the static mechanism is assumed to operate and, if the positive pressure phase is less than one-quarter of the characteristic period, then the plastic hinge mechanism is the governing mechanism. However, the demarcation is not distinct and, for the region where a quarter of the characteristic period and the positive pressure phase are approximately equal, either mechanism may occur and the resulting deformation and failure is strongly dependent on the shape of the pressure-time curve. General discussion of the response of circular plates subjected to impulsive loadings is given by Cristescu⁽¹⁾ and some later work is described by Johnson⁽²⁾ and Abrahamson⁽³⁾. The response of square or rectangular flat plates is a much more complicated phenomena, and several computer studies such as those by Kay⁽⁴⁾ and Huffington⁽⁵⁾ are available. Such preliminary results on response of flat plates subject to fuel-air explosive blast waves have been reported by the authors⁽⁶⁾ and a technical report concerned with this subject is in progress; therefore, further discussion on response of flat plates will be omitted from this report.

1.3 Previous Analyses of Beams

Some early work on beam response, resulting in plastic deformation, is that of Duwez, et al⁽⁷⁾ and is based on transverse impact of a concentrated load on an infinitely long beam. An elementary analysis of a free ended beam with central transverse impact was presented by Lee and Symonds⁽⁸⁾ at about the same time and the analysis is based on a rigid-perfectly plastic material. This assumption makes use of the fact that when a large amount of kinetic energy is available to produce

plastic deformation the plastic work in the beam far exceeds the elastic work. This assumption used in References 7 and 8 also leads to the use of a localized plastic deformation, commonly called a plastic hinge, as a means of describing the deflection process. The plastic hinge mechanism is not restricted to dynamic analyses and a general discussion of the mechanism and several applications to static problems is given by Timoshenko and Gere⁽⁹⁾. Due to the importance of the assumptions made in the use of a plastic hinge mechanism a general development will be given.

If the stress in a beam remains below the proportional limit, the beam behavior is independent of the shape of the plastic portion of the stress-strain curve of the material. When a beam is loaded in such a manner that the stresses exceed the proportional limit of the material the behavior of the beam in bending is then termed inelastic or plastic and is very dependent on the inelastic portion of stress-strain curve for the material.

The basic assumption used in this discussion is that once the entire portion of a beam cross section exceeds the proportional limit of the material a plastic hinge forms and any additional increase in loading will cause unrestricted rotation of the beam at this point. The plastic moment required to produce the plastic hinge is dependent on the shape of the stress-strain curve of the material. A discussion of the various stress-strain curve shapes and their resultant effect on the plastic moment and hinge will not be given here. The analysis as presented in this report will incorporate the use of the rigid-plastic model for ductile materials as shown in Figure 2. Non-ductile or brittle materials tend to act completely elastic and an analysis using a plastic hinge is not applicable. An elastic analysis may be found in a discussion of classical beam theory in texts such as Reference 9.

The plastic moment for a beam is also dependent on the cross-sectional shape of the beam and is readily determined in terms of the yield moment. The yield moment is the moment required to produce the yield stress at the outermost fiber of the beam cross section. Using the stress distribution of Figure 3a and integrating the first moment of stress over the beam cross section, the yield moment is found to be

$$M_Y = \int_A \sigma_Y \left(\frac{Y}{c} \right)^2 dA = \frac{S}{c} \sigma_Y \quad , \quad (1)$$

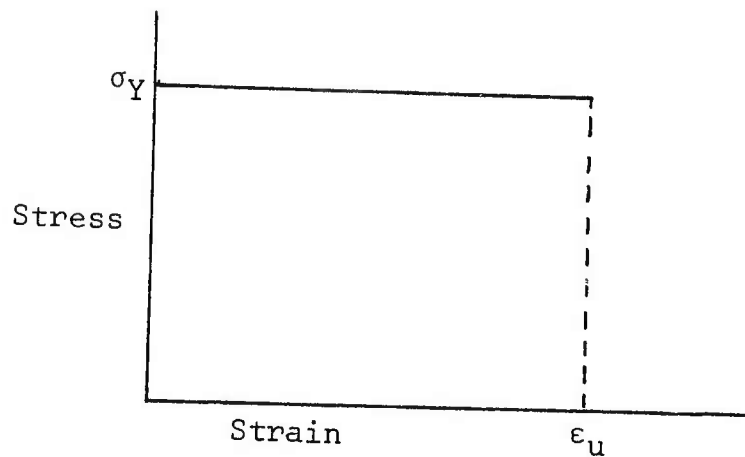


Figure 2. Idealized Stress-Strain Curve

where S is the planar moment of inertia of cross section about the bending axis and c is the distance from the beam centroid to the outermost fiber. Using Figure 3b the plastic moment may then be determined as

$$M_p = \int_A \sigma_Y y dA \quad . \quad (2)$$

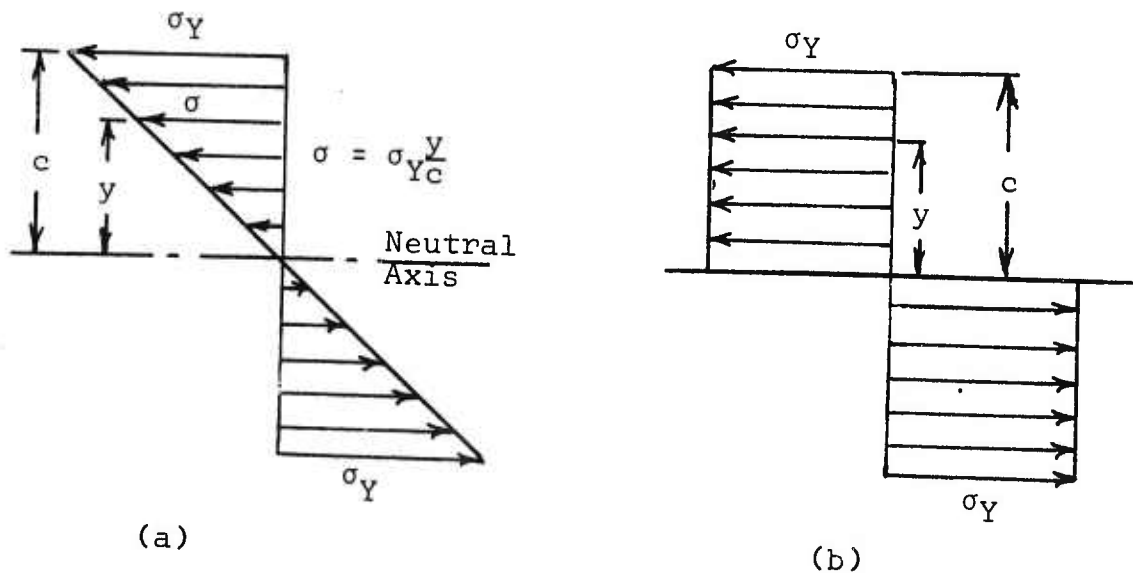






Figure 3. Bending Stress Distribution

The ratio of the plastic moment to the yield moment is solely a function of cross section shape and is defined as the beam shape factor,

$$f = M_P / M_Y \quad . \quad (3)$$

The value of f for various shapes is given below in Table 1.

TABLE 1. BEAM SHAPE FACTOR

| Shape | f |
|---|------|
|  | 2.00 |
|  | 1.70 |
|  | 1.50 |
|  | 1.15 |

The shape factor f for wide flange beams is typically in the range of 1.1 to 1.2 (Reference 9).

Using Equations (1) and (3) the plastic moment is written as

$$M_P = f \sigma_Y \frac{S}{C} = f \sigma_Y Z \quad ,$$

where Z is the section modulus defined as

$$Z = \frac{S}{C} \quad . \quad (4)$$

When the stress in the beam is such that plastic hinges form, the beam is assumed to act as a set of linkages free to rotate about the plastic hinge points. For example, if a simple supported beam is loaded statically, a plastic hinge will form at the midspan and rotation then occurs at the plastic hinge of

the midpoint and the natural hinges at the ends as shown in Figure 4. For a beam fixed at both ends, plastic hinges form at the fixed ends as well as at the midpoint. If true end fixity occurs such that the end points do not move axially, then tension is induced in the beam due to the deflection and increased length of the beam.

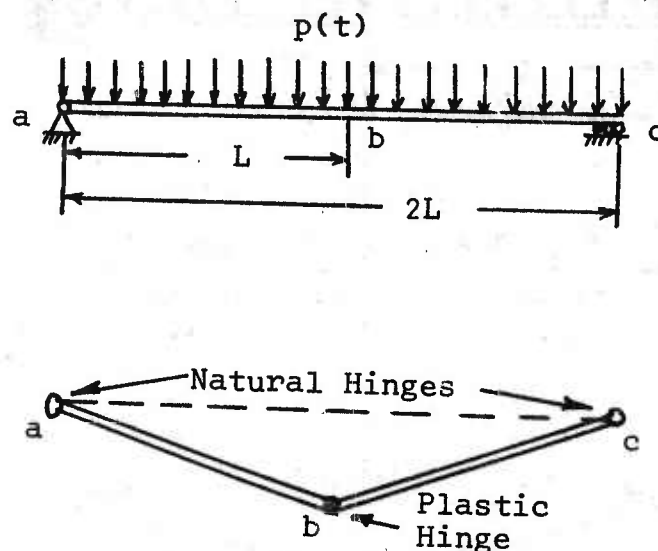


Figure 4. Static Beam Failure Due to Plastic Hinge

The dynamic response of a beam to impulsive loads may be described in terms of plastic hinges and for the case of low overpressure the mechanism may be the same as the static analysis. However, for high peak overpressures a traveling plastic hinge, as shown in Figure 5, forms and moves away from the beam end points. The intersection of the two moving plastic hinges is dependent on the beam end fixity. Once the traveling hinges intersect then the response is the same as that for the static case. The sequence for this mechanism is shown in Figure 5.

The loading condition governing which mechanism is in effect is based on the value of peak overpressure of the pressure time function, and Abrahamson, et al⁽³⁾ show that if the peak overpressure $p \leq 3p_0$, where p_0 is the static collapse pressure, then the static mechanism is valid. Thus, for $p > 3p_0$ a traveling hinge is present. A development and discussion of equations of motion for both the traveling and static mechanism in a beam

neglecting axial tension is given in Reference 3. A general discussion of the results of this reference follows.

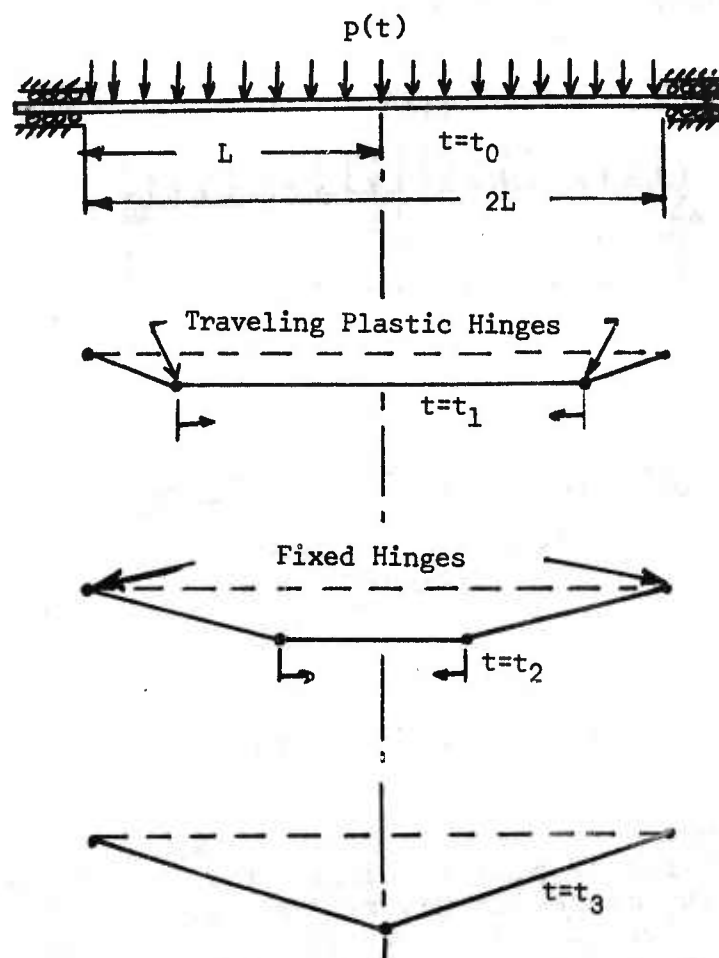


Figure 5. Moving Plastic Hinge Mechanism

The analysis of beam response as given in Reference 3 is divided into the classical static and plastic hinge mechanisms. The condition governing which mechanism holds is based on the peak overpressure of the loading function and is specified in terms of the static collapse pressure p_s . The static collapse pressure is determined from a static analysis assuming that a uniform pressure exists over the entire span $2L$ and plastic

hinges are operating with the only resisting force being the plastic moment M_p . Under these assumptions the static collapse pressure

$$p_s = 4M_p/L^2, \quad (5)$$

for the fixed end beam and

$$p_s = 2M_p/L^2, \quad (6)$$

for the simply supported beam. Using the above definition the static mechanism is assumed to hold if the peak overpressure p_m , as shown for a typical blast loading of Figure 6, falls in the range, $p_s < p_m < 3p_s$. If $p_m > 3p_s$ the traveling plastic hinge mechanism is assumed to operate.

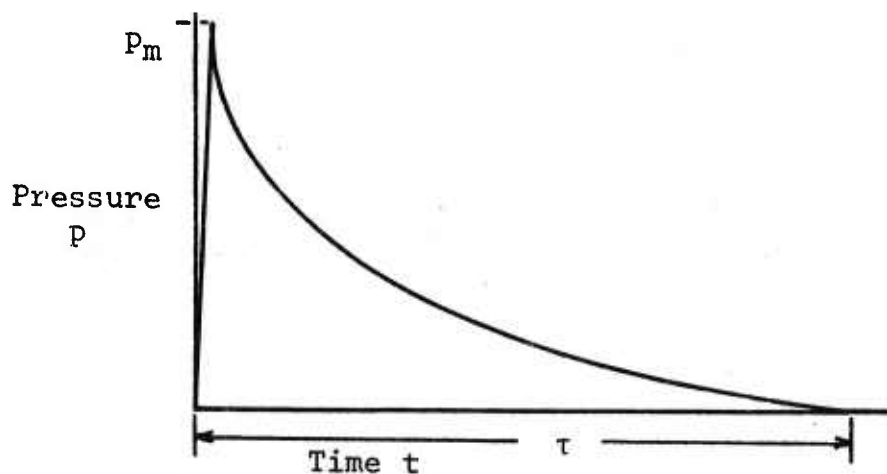


Figure 6. Typical Blast Pressure Time Curve for a Fuel-Air-Explosion

For a fixed end beam where end rotation is by a plastic hinge, an additional plastic hinge also forms at the center and the deflected shape is the same as Figure 4. The velocity of the midpoint is found to be

$$V = 3(\bar{I} - p_s t)/2m, \quad (7)$$

where m is the mass per unit length and \bar{I} is the impulse per unit length at the time t . The time t_2 where motion ceases

may be determined by setting Equation (7) to zero and integrating the resulting equation,

$$\bar{I}_2 = \int_0^{t_2} p(t) dt = p_s t_2 \quad . \quad (8)$$

where \bar{I}_2 is the value of the impulse at t_2 and for some cases may be determined by integration. The value of t_2 may be interpreted graphically, as shown on page 32 of Reference 3, for those cases where an analytical expression of the blast loading is not known. Knowing the time t_2 , the final midpoint deflection may be determined from the integration of the velocity expression over the time limits zero to t_2 . This integration yields the maximum center point deflection

$$y(L, t_2) = \frac{3}{2m} \left(\int_0^{t_2} \bar{I} dt - p_s t_2^2 / 2 \right) \quad . \quad (9)$$

The equations governing the static mechanism for a simply supported beam are the same as those of the fixed end beam except the static collapse load for this case is given by Equation (6).

Equations of motion for a fixed end beam with the traveling plastic hinge mechanism, as shown in Figure 7 and determined by Abrahamson et al⁽³⁾, are given as

$$m\dot{v} = p \quad , \quad x_h < x \leq L \quad . \quad (10)$$

and

$$mx_h^3 \dot{\omega} / 3 = px_h^2 / 2 - 2M_p \quad , \quad 0 \leq x < x_h \quad , \quad (11)$$

where p is the general expression for pressure as a function of time, x_h is the position of the plastic hinge, and ω is the angular velocity of the segment AB of Figure 7b. Using a continuity condition at the hinge point B of Figure 7a the velocity of the underformed portion BC may be expressed as

$$V = \omega x_h \quad , \quad (12)$$

With the use of Equations (11) and (12) the position of the plastic hinge x_h and its velocity \dot{x}_h are determined, respectively, as

$$x_h^2 = 12M_p t / \bar{I} \quad (13)$$

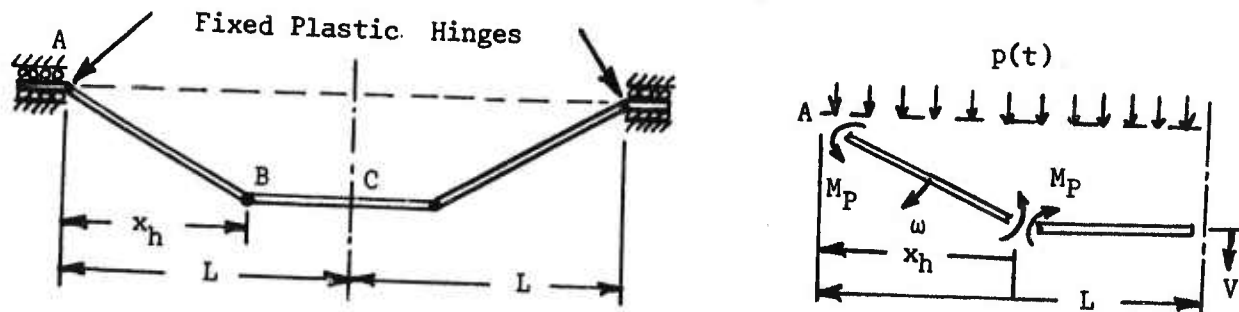


Figure 7. Traveling Plastic Hinge Mechanism and Free Body Diagram

and

$$\dot{x}_h = 6M_P(\bar{I} - pt)/\bar{I}^2 x_h \quad (14)$$

The time t_1 when the plastic hinges arrive at the center of the beam is determined by

$$\bar{I}_1 = \int_0^{t_1} p(t) dt = 3p_s t_1 \quad (15)$$

and in turn the centerpoint velocity V_1 and deflection $y(L, t_1)$ at time t_1 are given by

$$V_1 = \bar{I}_1/m \quad (16)$$

and

$$y(L, t_1) = \frac{1}{m} \int_0^{t_1} \bar{I} dt \quad (17)$$

Motion of the beam beyond this time t_1 is governed by the static mechanism and again if the velocity expression (7) is set to zero, the time t_2 , when motion ceases, is given by Equation (8). The final center point deflection is then given by the expression

$$y(L, t_2) = y(L, t_1) + \frac{3}{2m} \left[\int_{t_1}^{t_2} \bar{I} dt - \frac{p_s}{2} (t_2^2 - t_1^2) \right] \quad (18)$$

For a simply supported beam the equations of motion are the same as those of Equations (10) and (11) except that $-2M_p$ is replaced by $-M_p$ due to the operation of only one plastic hinge at the center of the beam.

As shown in Figure 7 the preceding beam analysis is based on a beam free of end constraints. This condition was taken into account in the design of an experiment described in Reference 3 to evaluate the preceding analysis. The experimental arrangement was such that the ends of the beam were fixed to sliding supports which permitted the beam ends to move toward each other and prevented a buildup of tension load. Uniformly distributed impulse values of 0.06 to 0.146 lb-sec/in were applied to 2024-T4 aluminum beams by use of thin strips of sheet explosive. The ratios of experimental centerpoint deflection to the theoretical values ranged between 0.402 and 0.652 for the pinned ends beams and 0.517 and 0.752 for the fixed ends beams with the higher ratios corresponding to the higher impulse loads. Although the analysis over-predicts the centerpoint, and may not be strictly applicable to beam analysis where tension is a factor, it does serve as an important guide to analytical methods using the plastic hinge mechanism.

Beam response to impulsive loads neglecting axial restraint was also studied by Symonds⁽¹⁰⁾ and in a later paper⁽¹¹⁾ he included the effect of axial restraint. In this study (Reference 11) the assumption of traveling plastic hinges was also used. However, in this case the central portion of the beam was given an initial velocity V_0 . The assumption of an initial velocity simplified the analysis and the final shape of the beam may be found somewhat easier than the preceding analysis. For the fixed end beam without axial restraint the final center point deflection $y(L, t_2)$ and rotation $\theta(L, t_2)$ along with support rotation $\theta(0, t_2)$ are found to be

$$y(L, t_2) = \frac{mL^2 V_0^2}{3(2M_p)} , \quad (19)$$

$$\theta(L, t_2) = \frac{mLV_0^2}{6(2M_p)} , \quad (20)$$

$$\theta(0, t_2) = \frac{mLV_0^2}{2(2M_p)} . \quad (21)$$

For the simply supported case without axial constraint the results are the same except $2M_p$ is replaced by M_p in Equations (19), (20) and (21).

An axial constraint was applied by Symonds⁽¹¹⁾ by adding an axial force N in addition to the moment M . A plastic axial force defined as

$$N_p = \int_A \sigma_Y dA \quad (22)$$

is assumed to be in effect when the entire beam cross section is subjected to the yield stress σ_Y . Using this definition, the plasticity condition

$$\frac{M}{M_p} + \frac{N^2}{N_p^2} = 1 \quad (23)$$

was imposed and must be satisfied for plastic deformation to occur. However, care must be used in applying Equation (23) to any cross section other than a rectangular section. In addition to Equation (23) a flow rule

$$\frac{N_p}{M_p} \dot{\epsilon} = 2 \frac{N}{N_0} \psi \quad (24)$$

defined in terms of strain rate $\dot{\epsilon}$ and curvature ψ was also imposed on the beam response analysis. Using the diagram of Figure 8 for a fixed end beam the equation of motion for angular acceleration of the segment AB about the point A is

$$\frac{1}{3} m x_h^3 \dot{\omega} = -2M - N y \quad (25)$$

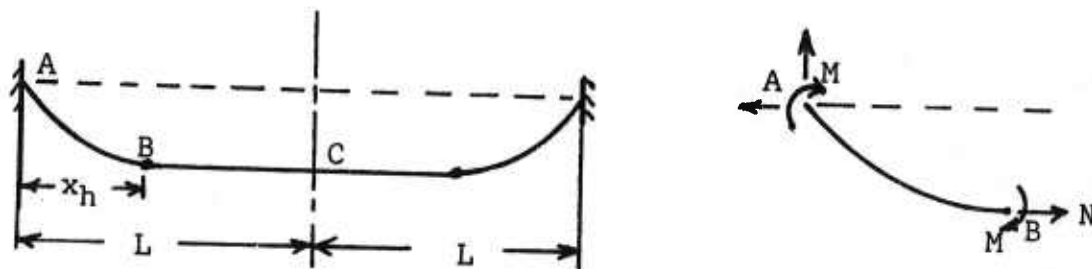


Figure 8. Beam Response Mechanism Including Axial Constraint

It can be shown from Equation (24) that the relation between linear strain and curvature becomes

$$\frac{N}{N_P} = \frac{N_P}{2M_P} \quad (26)$$

Using a velocity continuity such as Equation (12) and Equations (23), (25), and (26), the values of M , N , w , and x_h may be determined. Simultaneous solution of these equations yields a third degree equation in terms of the final center point deflection which can be given as

$$\frac{y_f}{L} + \frac{1}{12} \left[\frac{N_P L}{(2M_P)} \right]^2 \left[\frac{y_f}{L} \right]^3 = \frac{1}{3} \frac{m L V_0^2}{(2M_P)} \quad (27)$$

where y_f is the final center point deflection defined previously as $y_f = y(L, t_2)$. However, the final deformed shape, strain, and curvature functions require a numerical integration procedure. Again, the equation for final deflection of a simply supported beam is obtained by replacing $2M_P$ with M_P of Equation (27). The foregoing analysis is based on small deflections and is limited to deflections on the order of the depth of the beam; however, the important point found here is that the deflection based on a model with no axial constraint may be as high as four times the deflection based on a model including axial constraint. Symonds⁽¹¹⁾ also discusses a transition of the beam response of bending with axial restraint to that of a plastic string with end restraint. The assumption allows for calculation of deflections on the order of 1 to 10 times the beam depth and these deflections agree quite well with results presented in a later paper by Symonds and Jones⁽¹²⁾ which includes corrections for strain rate sensitivity. However, the deflections in these references are still quite small in comparison to gross deflections which would be expected to cause failure.

The majority of the previous researchers have avoided the treatment of beams for loads intense enough to cause failure from a structural standpoint. This is not to say that intense impulsive loadings have not been studied but much of the work in this area has been concerned with basic material problems rather than overall structural response. However, tearing and shear failures in explosively loaded clamped beams were studied by Menkes and Opat⁽¹³⁾ and a failure criterion based critical particle velocity is given by Sewell and Kinney⁽¹⁴⁾.

The results of the study of Reference 13 indicate that three separate damage levels occur as the strength of the impulsive load is increased. These damage modes listed in increasing impulse intensity are:

- 1) Large inelastic deformation described by a residual central deflection.
- 2) Tearing or tensile failure at the supports.
- 3) Transverse shear failure at the supports.

The threshold for mode 2 is taken as the impulse intensity which first causes tearing. As the intensity of the impulse increases, overlapping of modes 2 and 3 begins, until a well defined shear failure occurs and is characterized by no significant deformation prior to failure.

Upon examination of results of this work⁽¹³⁾ several main points were observed.

- 1) The final deformed shape of the beams subjected to the low impulse intensities indicates a static plastic hinge mechanism was in operation during the final deformation process.
- 2) The mode 2 failure may well be the result of tensile loads caused by excessive deflection occurring while mode 1 is operative. The authors of Reference 13 conclude that the mode 2 threshold is dependent on the same variables associated with prediction of central deflection of mode 1.
- 3) Mode 3 (shear failure) is dependent on the initial velocity and not shear stress and for a given material the threshold velocity is a constant.

The constant threshold velocity for a given material leads on to examine the new failure criterion presented by Sewell and Kinny⁽¹⁴⁾. They proposed that failure would occur if the initial velocity, defined in the manner of Equation (16), exceeded the tensile critical particle velocity⁽¹⁵⁾ of the material. This new failure criterion was applied to plate and beam elements when the positive pressure phase of the blast wave was less than one-quarter of the characteristic period of the structural element. However, it was found earlier by the authors⁽⁶⁾ that the shear critical particle velocity, as defined in Reference 16, gave better predictions than that of the tensile critical particle velocity in experiments involving failure of aluminum panels. A comparison of the shear failure threshold impulse reported in Reference 13 and that calculated using the shear critical particle velocity is given in Figure 9. The solid

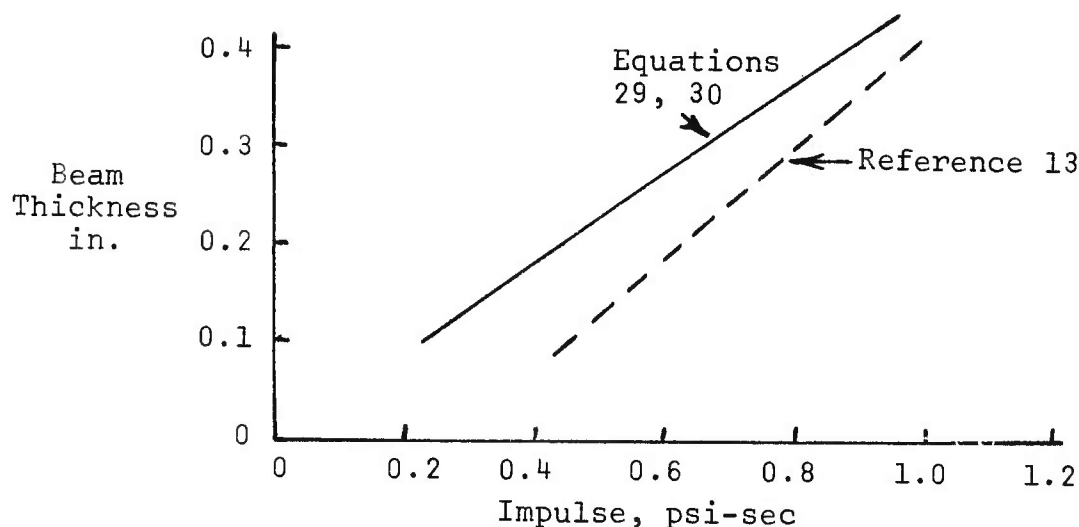


Figure 9. Impulse Required for Shear Failure Mode of Beams

critical impulse curve of Figure 9 is based on a shear critical particle velocity⁽¹⁶⁾ given as

$$(v_{CR})_s = (v_{CR})_T \left[\frac{2}{(v_{cr})_T} \sqrt{\frac{\sigma_u}{\rho}} - 1 \right]^{\frac{1}{2}} \quad (29)$$

where $(v_{CR})_T$ is the tensile critical particle velocity, σ_u is the ultimate tensile stress and ρ is material density. The corresponding critical impulse for shear failure is then

$$(I_{CR})_s = (v_{CR})_s mh, \quad (30)$$

where h is the beam depth. The tensile critical particle velocity for some aluminum alloys is approximately 220 ft/sec. by Rinehart⁽¹⁵⁾.

Based on the preceding discussion of previous work it is apparent a need exists for some analysis to predict gross deflections for mild impulse intensities found in fuel-air explosions. The next subsection is devoted to a strength of materials approach for predicting beam response in terms of plastic hinges and axial restraint with large deflections.

1.4 Response of Beams Subjected to a Fuel-Air Explosion

For loading functions of fuel-air explosions the positive pressure phase is rather long (millisecond range) and the shape of the pressure time function becomes important. It is then necessary to include the entire pressure time history and assume an initial velocity of zero in analyzing beam response to fuel-air explosions. The following discussion represents a development of a beam response model when subjected to a reflected pressure time history of a fuel-air explosion. The pressure is assumed to act uniformly over the width and length of the beam and it is further assumed that the end points of the beams are fixed against any movement toward each other. Both the fixed end beam, allowing no rotation except by plastic hinge, and the simple supported beam, allowing rotation by natural hinges, will be discussed. It is also assumed that the plastic energy is much larger than the elastic energy.

For the static case with both ends fixed against rotation, plastic hinges form at the center and ends of the beam and, using the diagrams of Figure 10, the energy and force functions needed for a Lagrangian formulation of the equation of motion may be written. Use of the Lagrangian method is justified by

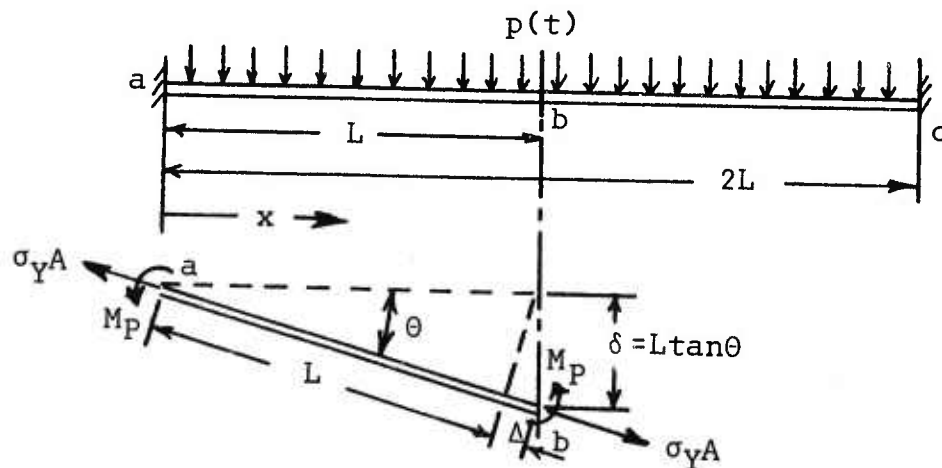


Figure 10. Free Body Diagram for a Static Analysis of a Beam Fixed at Both Ends

expressing the deformed beam shape in terms of the undeformed coordinate system and by writing the dissipative functions in terms of the plastic energy.

The following symbols will be used in the derivation of the equation of motion for the half span of Figure 6.

| | |
|----------------|--|
| A | cross section area of beam |
| L | half span length |
| M _P | plastic moment |
| M _Y | yield moment |
| S _a | moment of inertia of half span about the end, $S_a = \frac{\rho AL^3}{3}$ |
| I(t) | impulse-time function (psi-msec) |
| p(t) | pressure-time loading function (psi) |
| V | Velocity of midspan (in/sec) |
| w | width of beam (in) |
| δ | deflection of midspan (in) |
| Δ | deflection along beam longitudinal axis (in) |
| σ _y | yield stress (psi) |
| ρ | mass density |
| θ | angular rotation of beam (rad) |
| x,y | coordinate axes along original beam position. |

The kinetic energy KE may be written assuming a uniform linear velocity variation in the direction of longitudinal axis of the half span and is expressed as

$$KE = \frac{S_a \dot{\theta}^2}{2} + \frac{1}{2} \int_0^L \left(\frac{\dot{\Delta} x}{L} \right)^2 \rho A dx \quad . \quad (31)$$

Making use of the moment of inertia given above, Equation (31) reduces to

$$KE = \frac{\rho AL}{6} (\dot{\theta}^2 L^2 + \dot{\Delta}^2) \quad . \quad (32)$$

Now Δ and $\dot{\Delta}$ may be expressed as

$$\Delta = (\sec\theta - 1)L \quad (33)$$

and

$$\dot{\Delta} = (L \tan\theta \sec\theta) \dot{\theta} \quad (34)$$

Using Equations (32) and (34) the kinetic energy becomes

$$KE = \frac{\rho A L^3}{6} (1 + \tan^2\theta \sec^2\theta) \dot{\theta}^2 \quad (35)$$

The plastic energy PE is now written as

$$PE = 2M_p\theta + \Delta\sigma_y A \quad (36)$$

and using Equation (33) the plastic energy may be written as

$$PE = 2M_p\theta + (\sec\theta - 1)\sigma_y A L \quad (37)$$

The generalized force determined from the applied pressure force is expressed as

$$Q_\theta = \frac{\partial}{\partial\theta} \left[\int_0^L (\delta) \left(\frac{x}{L} \right) p(t) w dx \right] \quad (38)$$

Assuming no shortening of the span then

$$\delta = L \tan\theta \quad (39)$$

and the generalized force becomes

$$Q = \frac{p(t)L^2 w}{2} \sec^2\theta \quad (40)$$

Defining the Lagrangian L and the Lagrange equation as

$$L = KE - PE \quad (41)$$

and

$$\frac{d}{dt} \frac{\partial L}{\partial \dot{\theta}} - \frac{\partial L}{\partial \theta} = Q_\theta \quad (42)$$

the equation of motion becomes

$$\begin{aligned}
& \frac{\rho AL^3}{3} (1 + \tan^2 \theta \sec^2 \theta) \ddot{\theta} \\
& + \frac{\rho AL^3}{3} (\sec^4 \theta \tan \theta + \tan^3 \theta \sec^2 \theta) \dot{\theta}^2 \\
& + 2M_p + \sigma_Y AL (\tan \theta \sec \theta) = \frac{p(t)wL^2}{2} \sec^2 \theta .
\end{aligned} \tag{43}$$

Equation (43) is valid only for positive values of θ . The basic assumption is that a plastic hinge is in effect at the beginning of the beam motion. This means that at $t = 0$ the moment resulting from the initial blast loading must be large enough to overcome the internal resisting force $2M_p$. For Equation (43) a necessary condition to insure positive initial values of θ is that initial values of $\dot{\theta}$ be positive. This criterion may be met by the requirement that

$$\begin{aligned}
& P_{\max} \leq 4M_p/wL^2 \\
\text{or} \quad & P_{\max} \leq 4f\sigma_Y z/wL^2 .
\end{aligned} \tag{44}$$

The assumption is also made that the maximum value of θ is reached in the interval $0 < t < \tau$. If this assumption is not true then an equation with the right hand side or forcing function equal to zero would hold for this case. This case is omitted in that either maximum deflection or failure is expected to occur within the interval $0 < t < \tau$.

The strain induced in the beam due to this deflection is composed of an average axial strain obtained from Equation (33) and defined as

$$\epsilon_a = \frac{\Delta}{L} = (\sec \theta - 1) , \tag{45}$$

and a strain ϵ_θ at the outermost fiber at the plastic hinge points. An estimate of the magnitude of ϵ_θ will be made from the following simple analysis.

In the preceding analysis a plastic hinge was assumed to be concentrated at a point; however, in reality the hinge point is the position where the yield stress first extends over the entire depth of the cross section. Extending out from either side of the hinge point is a plastic zone of total length L_p as shown in Figure 11a. This zone is essentially a volume of the beam in which the internal stress is equal to the yield stress.

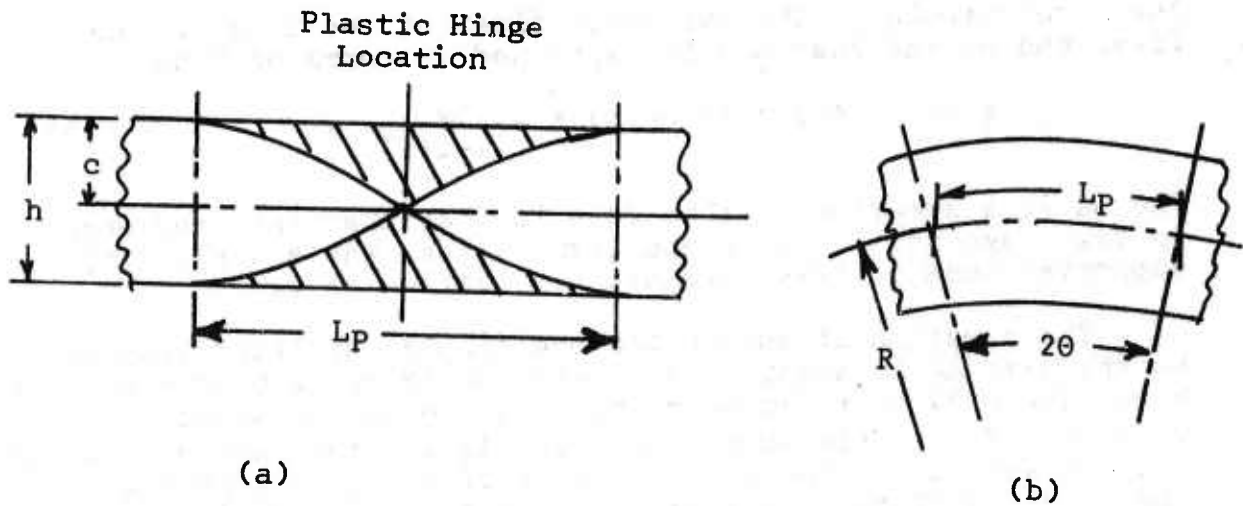


Figure 11. Schematic of Plastic Zone

The plastic zone length L_p as shown in Figure 10a is given in Reference 9 as

$$L_p = 2L(1-1/f) \quad , \quad (46)$$

where $2L$ is the beam span and f is the beam shape factor. Taking L_p as an arc length corresponding to the angle 2θ and radius of curvature R of Figure 11b the strain may be determined from

$$\epsilon_\theta = \frac{c}{R} \quad . \quad (47)$$

The radius of curvature R is then

$$R = \frac{L_p}{2\theta} \quad (48)$$

and substituting Equations (46) and (48) into Equation (47) gives the strain due to rotation as

$$\epsilon_\theta = \frac{c\theta}{L(1-1/f)} \quad . \quad (49)$$

Defining strain ϵ as

$$\epsilon = \epsilon_a + \epsilon_\theta \quad , \quad (50)$$

the total strain at the outermost fiber of the midpoint and fixed end of the beam may be expressed in terms of θ as

$$\epsilon(0) = \epsilon(L) = (\sec\theta - 1) + \frac{c\theta}{L(1 - 1/f)} \quad (51)$$

The basic assumption in this case is that the fixed end beam is fixed against rotation and translation, whereas the simple supported beam is fixed against translation only.

The equation of motion for the simple supported beam will be the same as Equation (43) except the third term of the right-hand side will be replaced by M_p . The resulting strain for the midpoint of a simple supported beam will be the same as Equation (51); however, for the support point of a simple supported beam the strain will be only $(\sec\theta - 1)$, due to the operation of a natural hinge at the support.

Solution of Equation (43) was obtained using a fourth order Runge-Kutta analog simulation program. Solutions were determined for 6061-T6 aluminum beams of the same size as those of Reference 13. Maximum strain values were determined using Equation (51) and any strain exceeding 0.15 was assumed sufficient to cause failure. Results of these calculations along with the experimental and theoretical results of Reference 13 are listed in Table 2. Experimentally determined pressure time functions of Reference 6 were used as an applied load $p(t)$ of Equation (43).

Applying the same general approach to that of a traveling plastic hinge as shown in Figure 12, the kinetic energy may now

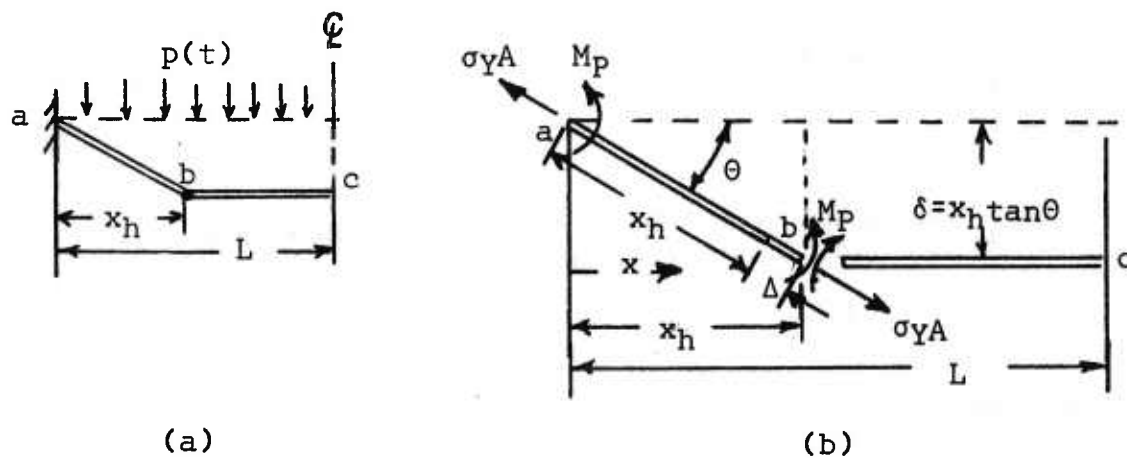


Figure 12. Schematic of Traveling Plastic Hinge Mechanism

TABLE 2. BEAM RESPONSE TO IMPULSIVE LOADS

| Impulse Ktaps | Beam | | Central Deflection | | |
|-------------------|--------------------|-----------------------|--------------------|-----------------|-------------------------|
| | Length (Inches) | Thickness (Inches) | Reference 13 | | Equation 43 (Inches) |
| | | | Theo (Inches) | Exp (Inches) | |
| 10.9 | 8 | 0.187 | 0.99 | 0.94 | + |
| 15.3 ^a | 8 | 0.187 | + | + | 0.769 |
| 17.8 | 8 | 0.187 | 1.56 | 1.44 | + |
| 10.9 | 8 | 0.250 | 0.54 | 0.50 | + |
| 15.3 ^a | 8 | 0.250 | + | + | 0.475 |
| 17.8 | 8 | 0.250 | 1.07 | 1.50 | + |
| 15.3 ^a | 8 | 0.375 | + | + | 0.154 |
| 17.8 | 8 | 0.375 | 0.72 | 0.50 | + |
| 10.9 | 4 | 0.187 | 0.44 | 0.25 | + |
| 15.3 ^a | 4 | 0.187 | + | + | * |
| 17.8 | 4 | 0.187 | 0.77 | 0.69 | + |
| 10.9 | 4 | 0.250 | 0.32 | 0.31 | + |
| 15.3 ^a | 4 | 0.250 | + | + | * |
| 17.8 | 4 | 0.250 | 0.53 | 0.44 | + |
| 15.3 ^a | 4 | 0.375 | + | + | * |
| 17.8 | 4 | 0.375 | 0.48 | 0.18 | + |

*No response

+No calculation or value

^aThis value calculated from experimentally determined pressure time curve for a fuel-air explosion given by

$$p(t) = 830(1-t/.0015)e^{-t/.0015}$$

be expressed in terms of the angle θ and the plastic hinge position x_h . Assuming that the central portion of the beam BC of Figure 12a remains rigid and resists the loads $\sigma_y A$ and M_p without deformation, the kinetic energy KE and the plastic energy PE may be defined in a manner similar to Equations (31), (32), (33), (34), (35), (36) and (37). The plastic energy in this case is the same as Equation (37) except L is replaced with x_h . An expression for the kinetic energy must now include a term for the central portion of the beam as well as the portion of length x_h . The expressions for the energy terms are found to be

$$\begin{aligned} KE = & \frac{\rho A x_h^2}{6} [x_h(1+\tan^2\theta \sec^2\theta) + 3(L-x_h)\sec^4\theta]\dot{\theta}^2 \\ & + \rho A x_h [(L-x_h)\sec^2\theta \tan\theta]\dot{x}_h\dot{\theta} \\ & + \frac{\rho A}{2} [(L-x_h)\tan^2\theta]\dot{x}_h^2 \end{aligned} \quad (52)$$

$$\text{and } PE = 2M_p\theta + (\sec\theta - 1)\sigma_y A x_h \quad (53)$$

Using the continuity of deflection at point B of Figure 12, $\delta = x_h \tan\theta$, the force component expression for the two coordinates and x_h may be determined. Using the total work done by the pressure force the force components are

$$\begin{aligned} Q_\theta &= x_h \left(L - \frac{x_h}{2} \right) w p(t) \sec^2\theta \\ \text{and} \quad Q_{x_h} &= (L - x_h) w p(t) \tan\theta \end{aligned} \quad (54)$$

Using Equations (41), (42), (52), (53) and (54) the equations of motion may be determined and are given as

$$\begin{aligned} & \rho A [(L-x_h)\tan^2\theta]\ddot{x}_h + \rho A x_h [(L-x_h)\sec^2\theta \tan\theta]\ddot{\theta} \\ & + 2\rho A [(L-x_h)\sec^2\theta \tan\theta]\dot{\theta}\dot{x}_h \\ & + \rho A x_h \left[\left(2L - \frac{5}{2}x_h \right) \sec^2\theta \tan^2\theta + \frac{x_h}{2} \sec^4\theta - \frac{x_h}{2} \right] \dot{\theta}^2 \\ & - \frac{\rho A}{2} [\tan^2\theta]\dot{x}_h^2 + \sigma_y A (\sec\theta - 1) \\ & = p(t)w(L-x_h)\tan\theta \end{aligned} \quad (55)$$

and

$$\begin{aligned}
& \rho A x_h^2 \left[\frac{x_h}{3} (1 + \tan^2 \theta \sec^2 \theta) + (L - x_h) \sec^4 \theta \right] \ddot{\theta} \\
& + \rho A x_h [(L - x_h) \sec^2 \theta \tan \theta] \ddot{x}_h \\
& + \rho A x_h [x_h (1 + \tan^2 \theta \sec^2 \theta) + (2L - 3x_h) \sec^4 \theta] \dot{\theta} \dot{x}_h \\
& + \rho A x_h^2 \left[2(L + x_h) \sec^4 \theta \tan \theta + \frac{x_h}{3} (\tan \theta \sec^4 \theta + \tan^3 \theta \sec^2 \theta) \right] \dot{\theta}^2 \\
& - \rho A x_h [\sec^2 \theta \tan \theta] \dot{x}_h^2 + 2M_p + \sigma_y A x_h \sec \theta \tan \theta \\
& = p(t) w x_h \left(L - \frac{x_h}{2} \right) \sec^2 \theta .
\end{aligned} \tag{56}$$

No attempt was made to obtain a solution to these equations.

1.5 Conclusions

Beam response mechanisms for failure are well defined at the extreme ends of the loading spectrum, with classical beam deflection modes to failure occurring at the static case and failure without deflection occurring at the very intense step loading case. Mechanisms associated with loadings between the two extreme cases are very dependent on the shape, pressure magnitude, and duration of the loading. As the loading becomes slowly time dependent the classical vibratory response becomes evident until such a point when the positive pressure phase of the loading is less than one-quarter of the characteristic period of the structure. When this happens the mechanism of response becomes one of the traveling plastic hinges associated with propagation of stress waves. As the impulse intensity continues to increase, a point is reached where the material simply cannot respond to the velocity of the impinging shock front and failure at the boundaries occurs without deformation of the central portion. The response in the transition regions between these rather distinct mechanisms are difficult to model. Response of beams and plates to fuel-air explosions fall in the transition region between vibratory response and stress wave response.

Small ductile beams subject to blasts of fuel-air explosion with fixed or pinned ends may not be modeled as pure bending, and tensile load due to the end constraint must be taken into account in analytical calculations. A rigid-perfectly plastic

material constitutive relation may be used when the plastic energy is very large in comparison to the elastic energy. For rather flexible beams the static mechanism will be sufficient to predict failure; however, a traveling hinge mechanism more than likely is responsible for the initial deflection. Due to the difficulty and complexity encountered in modeling beam response to fuel-air explosions a program of testing and empirical analysis may be in order. Tests of beams and plates stiffened with beam elements subjected to actual fuel-air explosions (bag experiments) are recommended.

SECTION II

FUEL-AIR EXPLOSION (FAE) IN CONFINED STRUCTURES

2.1 Introduction

Before considering the effects of fuel-air explosions in large closed or confined areas a discussion of the fuel-air explosion in unconfined areas is in order. For a given fuel-to-air mixture many of the characteristics found in a fuel-air explosion are applicable whether the gas cloud is in a large container or open to the atmosphere.

2.2 Fuel-Air-Explosion

A fuel-air explosion is a rather complicated phenomena; however, in broad simple terms of explanation: given a proper fuel-to-air mixture and a small high energy secondary explosion at some point or line in the mixture, a detonation wave is established and moves through the fuel-air mixture at some constant velocity. Under the proper conditions the wave behaves like a strong blast wave but later it may be described as a Chapman-Jouguet⁽¹⁷⁾ detonation wave. The velocity, pressure, temperature, and density changes across the wave are all step functions as in the case of a strong shock wave in air; however, in the case of the detonation wave they are all constant with time and depend only on the properties of the fuel-air medium ahead of the shock. The basic difference between the detonation wave and the regular shock is that the energy equation for the detonation wave has a term which represents the heat liberated in the reaction zone and is added to the energy flux passing through the reaction zone⁽¹⁸⁾. This heat addition coming at the wave front causes a larger temperature jump than that of a regular shock. In turn, this increased temperature increases the acoustic velocity and decreases the particle velocity behind the front.

The wave may be planar, cylindrical or spherical, depending on the type of secondary detonation. The static or side-on pressure jump across the wave is the same in all three and is constant with time. Only the shape of the wave behind the front is changed with time or distance from the secondary explosion source and is highly dependent on distance to the nearest relief surface. For a strong detonation wave the static or side-on pressure ratio of pressure across the wave front is given by

$$\frac{P_1}{P_0} = \frac{\rho_0 D^2}{\gamma_0 + 1} = \frac{1 + \gamma_0 D^2}{\gamma_1 + 1} \quad (57)$$

where

- P_0 - static pressure in medium ahead of the wave (psi)
- P_1 - static pressure at wave front (psi)
- ρ_0 - density in medium ahead of the wave (lb-sec²/in⁴)
- D - wave front velocity (in/sec)
- γ_0 - ratio of specific heats in front of detonation wave
- γ_1 - ratio of specific heats behind detonation wave.

The reflected pressure p_r exerted on a rigid wall given in Reference 18 for a condensed explosive and verified experimentally by Ross and Strickland⁽¹⁹⁾ for a fuel-air mixture may be expressed in terms of the side-on pressure as

$$\frac{P_r}{P_1} = \frac{5\gamma_1 + 1 + \sqrt{17\gamma_1 + 2\gamma_1 + 1}}{4\gamma_1} \quad (58)$$

As shown in Equation (58) the ratio of reflected pressure to the side-on pressure is dependent only on the ratio of specific heats and is fairly insensitive to changes in values of γ above unity. The value of p_r/p_1 is 2.6, 2.4 and 2.3 for γ values of 1, 3 and ∞ , respectively. This indicates that the reflected pressure will be about 2.4 times the static pressure for almost any fuel-air mixture. Further observations for fuel-air explosions⁽¹⁷⁾ show that for most fuel-air mixtures the detonation velocities are approximately 5000 to 6000 FPS. This means that for almost any fuel-air explosion the reflected pressure is nearly a constant and will be much lower than that of a reflected shock wave in air with the same static pressure rise.

The static pressure rise and corresponding reflected pressure given by Equations (57) and (58) were verified experimentally⁽⁶⁾ for a MAPP-Air system. Impulse calculations based on the experimental pressure time histories also check with analytical predictions of Sichel and Hu⁽²⁰⁾. Analytical predictions of fuel-air explosions are given by Nicholls, et al^(21,22) and the reader is referred to these documents for further discussion of unconfined fuel-air explosions in the atmosphere.

2.3 Confined Fuel-Air Explosions

In the previous section a fuel-air explosion was defined in terms of a detonation wave traveling through a fuel-air medium. One of the major assumptions was that the fuel-air cloud was of sufficient size and mixture to produce a strong detonation shock. For the confined case the assumption will be that the limits of the confinement are large enough such that the same conditions are satisfied to produce a detonation wave, and the mechanism will be the same as the unconfined case.

In the case of unconfined fuel-air explosions the ground impulse and the dynamic or reflected impulse are often the parameters used to describe the damage capability of the explosion. It is assumed that this will also be true for the confined fuel-air explosion. In the analysis of an idealized unconfined fuel-air explosion⁽²²⁾ it was assumed that no side or top relief occurred. This is essentially the same assumptions that would be used in the analysis of a confined fuel-air explosion. This analysis gives a typical side-on pressure time history or shape as shown in Figure 13. The effect of confinement on a FAE is to maintain some high pressure for some finite time as evidenced by the plateau of the pressure time curve shown in Figure 13. In the unconfined case a relief wave moving at the acoustic speed in the burned gas quickly reduces the pressure behind the detonation wave and the resulting pressure time curve is similar to that of Figure 6. For a confined FAE, the reflected pressure profile will be similar in shape to that of Figure 13 except the peak overpressure will be approximately 2.4 times that of p_1 . The ground impulse and dynamic or reflected impulse as calculated in References 20 to 22 will be applicable to fuel-air explosions in buildings, aircraft shelters, hangers, etc. In such cases a detonation wave whose shape depends on location and size of the secondary explosion will move through the medium at a constant velocity and be reflected from the walls and/or top.

The wave type, i.e., planar, cylindrical, spherical, will depend on the general shape of the building and type and location of secondary explosion. For rather long buildings there will be a tendency to form a planar wave as the detonation front moves down the length of the structure. In this case the major damage would be caused at one end due to the reflection of the wave. In most buildings roof lift may be the most vulnerable mechanisms and in such cases an initiator or second event charge on the floor would give wave reflection at the roof or overhead. Due to the rather small peak overpressure of FAE devices, it is essential to try and direct the wave in

such a direction as to cause the most damage. Of course, this may be impractical to do and in turn calculation of the exact pressure or impulse at a point inside the structure may not be possible even if the exact location of the secondary blast was known.

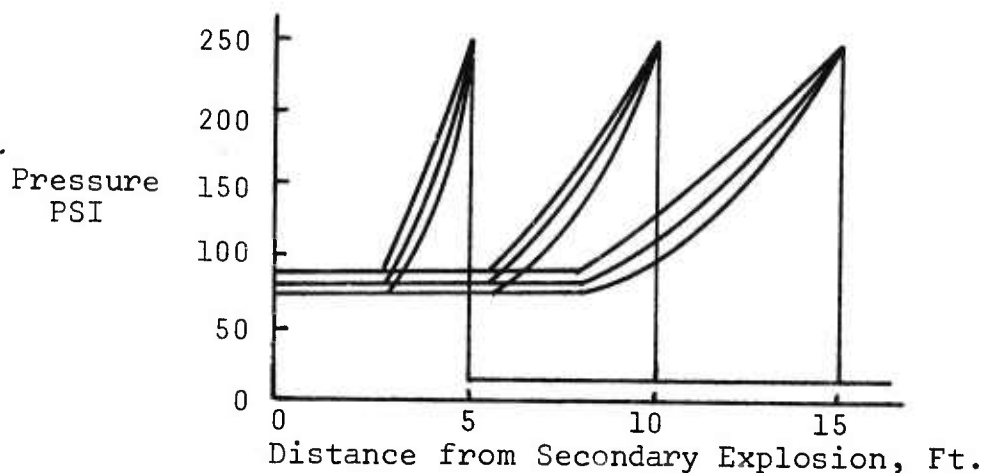


Figure 13. Pressure of a Fuel-Air Explosion Versus Distance from the Secondary Explosion

For point secondary explosions or initiators a spherical wave will be established and if the geometry of the reflecting surface is given a reasonable estimate of the impulse may be determined based on calculations of Reference 20.

2.4 Conclusions

Reflected pressures of fuel-air explosions from rigid walls will reach a maximum of approximately 2.4 times the static pressure rise of the detonation wave. The same detonation wave mechanism of unconfined fuel-air explosions without edge relief will be operative for fuel-air explosions in large unpressurized containers. As in the case of unconfined fuel-air explosions the main damage mechanism for large structures will be the reflection of a detonation from the walls, top, or end of the confining structure. For confined explosions where failure occurs pressure relief will occur upon venting and the effect of this pressure relief should be taken into account when calculating the impulse intensity or positive pressure phase of the detonation wave.

SECTION III

STRUCTURAL DEGRADATION OF CONCRETE BY IMPULSIVE LOADS

3.1 Introduction

This phase of the research was intended to follow up specific areas of interest to the sponsor. A briefing at Eglin AFB on 3 and 4 January 1974 led to the suggestions that any predictive formulas for (1) crater shape and material removal caused by explosive surface loading on a semi-infinite half-space of concrete, or (2) spall or corner failures in finite concrete slabs, blocks and beams would be of value. Alternatively to concrete studies, investigations of rock aggregates were considered to be of interest to the Air Force.

In the following investigation, covering a period of about six months, two areas received most of the attention: (1) a literature survey and laboratory visits to compile information primarily on cratering, and (2) an experimental laboratory study of dynamic tensile fracture of concrete bar specimens⁽²³⁾. Some results of the experimental study are reported in Section 3.4.

A compilation of places visited and conferences attended is given in Appendix A.

The cratering process will be described in the remainder of this introduction. Section 3.2 then considers empirical cratering formulas. Section 3.3 refers briefly to some more fundamental approaches seeking to obtain, for brittle materials like rock and concrete, equations of state or constitutive equations that can be used in two-dimensional codes to calculate the details of cratering and penetration.

Figure 14 is a schematic half-crater profile from a near-surface explosion in a rock medium. The figure indicates regions of more or less violent deformation and defines the symbols for height of burst (HOB), measured to the mass center of the charge, and the apparent and true crater radii and depths. The dissociated material (fallback and ejecta) consists of some fine-grained material and some larger blocks or chips. The boundary of the true crater, separating this dissociated material from the rupture zone, is not always precisely defined, since some of the material in the rupture zone can sometimes be removed with very little effort. Also the two boundaries, separating the zone of slight rupture and fracture

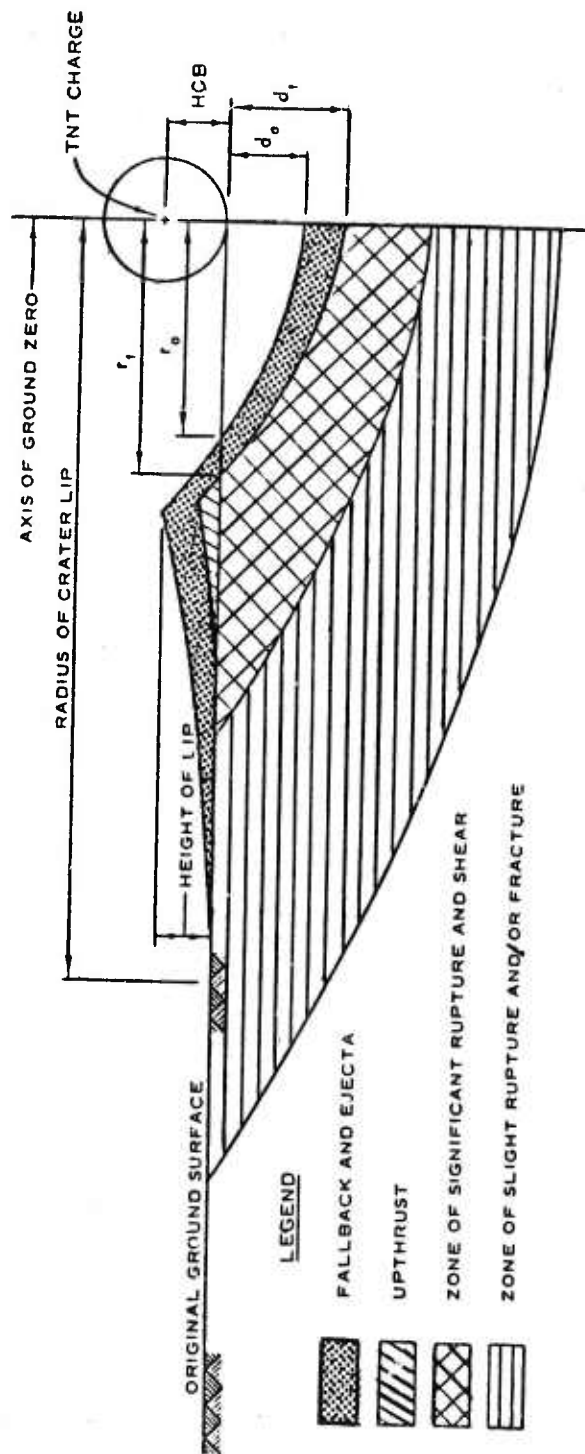


Figure 14. Typical Half-Crater Profile from a Surface or Near-Surface Shot Over a Hard Rock Medium (After Davis(24))

from the zone of significant rupture and shear and from the elastic region below, are gradual transitions rather than sharp boundaries. In softer rocks and soils the zones here called rupture zones are often referred to as the plastic region (to distinguish it from the elastic region below).

Broberg⁽²⁵⁾ has reported results of contact detonations (with charge masses up to 1000 kg on granite slabs). He characterized three regions somewhat differently:

(1) First is the powder zone or crushed zone directly below the charge, where the compressive stress transmitted greatly exceeds the compressive strength of the material.

(2) Between the powder zone and the initial position of the true crater boundary lies the block zone, where failure is due to tensile and shear stresses, producing blocks or chips.

(3) Below the true crater boundary is the rupture and shear zone of nonelastic action, and below that the elastic region.

Broberg's data indicated that the final true crater was roughly conical with $d_t = 0.33r_t$. (M. P. White⁽²⁶⁾ in 1946 suggested the relation $d = 0.4r$ for the approximately conical craters produced by contact explosions on concrete.)

Kaplan⁽²⁷⁾ has reported on the effect of material properties on crater dimensions and shape. Lead azide charges (0.9 to 24 grams) were detonated in true surface-shot geometries on blocks of grout of varying properties. Crater depths decreased sharply, due to a reduction in crushing and compacting, when the compressive strength reached about 1000 to 1500 psi (6.89 to 10.3 MN/m²). For low strengths the craters were almost hemispherical. As the strength was increased the lower part of the crater remained hemispherical while the upper portions flattened. At still higher strengths the hemispherical bottom gradually disappeared until the entire crater was either dish shaped or a flat conical shape. Both this study and that of Broberg on granite point up the increasing importance of (front-face) spalling in crater formation as the material strength increases.

The most extensive studies of cratering from explosives have been in connection with nuclear explosives and the attempts to model their effects by chemical explosives (HE). Most of these studies⁽²⁸⁻³⁶⁾ have been concerned with buried explosions. Any further study concerned with cratering after partial penetration in concrete could profit from consulting this literature and also the extensive blasting research literature in connection with mining and excavation technology⁽³⁷⁻³⁸⁾.

Section 3.2 considers the modeling of surface and near surface shots in rock and concrete. Most of the information given is for rock rather than concrete, because that is what is available. It is believed that the same procedures can be applied to concrete if sufficient experimental data can be obtained.

3.2 Empirical Cratering Formulas for Surface and Near Surface Shots

3.2.1 Preliminary Comments

This part of the investigation addressed the question of whether it is possible to predict the crater volumes and dimensions produced by surface explosions on massive concrete blocks or slabs by the use of simple empirical formulas. Not enough experimental data on concrete was found to test the empirical formulas, but there are several reports on cratering in rock by HE, both from blasting research related to mining and excavation and from extensive studies of the modeling of nuclear explosive loading by HE experiments. These results lead to the conclusion that cratering in concrete could be modeled in the same manner.

The empirical formulas have quite successfully represented true crater dimensions as a function of charge weight over a range of one pound to 100 tons, provided that the material was reasonably homogeneous (no large faults or layers of different material) and that the surface contact conditions and charge shape and detonation initiation position were maintained the same. The nuclear explosive modeling encountered difficulties with extension up to the megaton range⁽³³⁾, but the model studies themselves showed remarkable consistency.

It is recognized that successful empirical representation of controlled-contact-condition surface-burst loadings will be of limited value for practical prediction of damage from bombs. Surface explosive attack is not an efficient way to remove material. A buried charge is much more effective, and there is an optimum depth of burial for a given charge and a given material. To maximize material removal by cratering one would seek to have the bomb penetrate to the optimum depth before exploding. This introduces a host of problems concerned with projectile design and fuzing and shaped charge design for effective penetration which are not considered in this report.

The 1974 Waterways Experiment Station compendium(33) comments, "It does not appear sufficient to predict bomb/shell crater dimensions from those formed by bare charges equivalent in yield to the bomb or shell filler material, even though it may be argued that explosive energy lost in rupturing the case is regained in the kinetic energy of the fragments. The explosive filler is usually cast in a cylindrical configuration, and detonation is usually initiated in the nose or tail of the warhead; these considerations also fail to answer completely the questions raised over differences in craters.

"The limited study which has been done on this subject indicates that deeply buried bombs produce craters smaller in radius but larger in depth than do comparable bare charges. There do not seem to be sufficient data on shallowly buried bombs to permit conclusions. Experience with mortar and artillery shells, which contain a proportionately heavier casing, indicates that near surface (fuze quick) bursts form craters which are somewhat larger than those of bare charges. Unfortunately, a complete resolution of this problem is hampered by a lack of definitive test data..."

The importance of the surface contact conditions and detonation initiation conditions has been well documented. For example, White (Reference 26, Chapter 15) mentions tests on concrete plates using demolition blocks on end and detonated either at the top or at the bottom. The total impulse transmitted to the plate was only about 4 percent greater for detonation at the top, but the crater volumes in concrete were nearly quadrupled over those for base initiation. The same report proposed the relationship $\bar{V} = 1.5J$ between crater volume \bar{V} (in³) and total impulse J (lb-sec) for normal concrete (compressive strength about 4000 psi) for charges on end detonated at the end away from the slab, but warned that the serious scattering of the data indicates that other effects are important. The scatter mentioned was even for fairly well controlled conditions. Bomb drop contact conditions would not be known so well.

More recent studies have further emphasized the importance of contact conditions. For example, Haas and Rinehart(39) report laboratory studies of the coupling from small unconfined and partially confined cylindrical charges (several grams) to uniform blocks cut from slabs of Yule marble. They explored the effects of

- (a) Length and diameter of the charge
- (b) Obliquely oriented charge

- (c) Partial confinement (i.e., partial insertion into a hole drilled in the rock)
- (d) Attenuation with distance in the rock, and
- (e) Coupling through layers of water, drilling mud, rock, aluminum, plexiglass, vermiculite, sand, foam rubber, or air.

The effects of diameter (or contact area), confinement and coupling material were especially noteworthy. The cylindrical charges were formed by stacking discs of DuPont EL-506A.

The peak stress at 2-inch depth for 0.5-inch-diameter charges increased from 26,500 psi for a 0.25-inch-long charge to 34,000 psi for 1.5-inch-long charges, with no further increase for 3-inch lengths. This is not a large increase, considering that the 1.5-inch-long charge weighed six times as much as the 0.25-inch-long charge. The constancy of the peak stress for charge lengths greater than 1.5-inch was explained by Haas and Rinehart from considerations of detonation head theory. For an unconfined cylindrical charge detonated from one end, a stable detonation head is formed by the time the detonation front has propagated approximately three charge diameters. Making the charge longer (for a fixed diameter) does not increase the peak stress propagated.

A measure of the attenuation of the peak stress with distance of travel was obtained by varying the slab thickness and measuring the momentum per unit area transmitted to a small pellet at the back face of the slab. For the 0.5 x 1.5-inch charge the peak stress in the rock dropped from 271,000 psi at 0.5-inch-depth to about 80,000 psi at 1 inch, 34,000 psi at 2 inches and 15,200 psi at 4 inches. This decay is considerably faster than the $1/r$ decay curve that would be predicted for a spherical elastic wave from a point source, especially between 0.5 inch and 1 inch.

The peak stress transmitted to a given distance of 2 inches (from a 1-inch-long charge) was strongly dependent on the charge diameter, increasing from 8010 psi for a 0.27-inch diameter to 61,700 for a 0.75-inch diameter. This was attributed to two factors. The duration of the applied pressure is greater for the larger diameter (1.4 microseconds for 0.75 inch compared to 0.5 microsecond for 0.27 inch). The longer pulse increases the extent of crushing near the charge. The shock wave peak stress emerging from the crushed region was said by Haas and Rinehart to be equal to the dynamic compressive strength of the rock. For a larger crushed region there is a shorter attenuation distance

from the point where the peak stress is equal to the crushing strength to the measurement point at 2 inches from the charge. The second factor involved in the dependence on diameter is that the larger diameter charge behaves less like a point source, so that the propagating wave front is flattened and shows less effect of spherical divergence at the 2-inch distance.

It may be noted that the experiments did not explicitly test the hypothesis that the peak stress in the wave emerging from the crushed region is independent of the size of the crushed region and equal to the dynamic compressive strength of the rock. If there is in fact a reasonably well-defined dynamic crushing strength expressed in terms of the radial stress in a spherical wave, then no higher stress will propagate out of the crushed zone, since, by definition, any higher stress would produce further crushing. The question is important because, if:

- (1) the extent of the crushed region can be predicted by simple scaling laws, and
- (2) the peak stress in the shock wave emerging from the crushed region is known without detailed knowledge of the constitutive equation governing the crushing,

then there is a possibility of estimating the stress level that will arrive at the back face of a slab and therefore of predicting back-face scabbing without a complete analysis of the wave propagation from front face to back face. (It should be noted, however, that the crushed region is not in general identical to the true crater estimated by the empirical laws to be discussed in the following subsection, since the true crater includes also the large blocks and chips loosened by the release wave after the initial compressive waves have passed.)

An air gap between the end of the 0.5 x 1.5-inch charge and the marble decreased the peak stress transmitted to the 2-inch depth from 33,800 psi for direct contact to about 24,000 psi for a 1/8-inch gap, 21,600 psi for a 1/4-inch gap and 12,200 psi for a 1-inch gap. Partial confinement by insertion of the 1.5-inch-long charge into a drilled hole only 0.5 inch deep almost doubled the peak stress transmitted to 2 inches from the end of the charge. These controlled-condition observations emphasize the problem of predicting the effect of bomb explosions when the contact conditions are not accurately known.

The importance of the contact conditions is also shown in the scaling of the surface bursts reported in Section 3.2-2. It is necessary to distinguish between so-called true surface bursts, where the charge is half buried with the mass center of the charge at ground level, requiring a prior hemispherical excavation for emplacement of spherical charge, and the surface-tangent charge configuration, where the mass center of a spherical charge is at a height of burst (HOB) equal to one charge radius r_c .

3.2-2 Scaling Laws and Empirical Formulas for Cratering

If geometric similarity is maintained by the craters produced in a given material by charges of varying size, then each linear dimension of the crater is proportional to the cube root of the volume. If in addition the crater volume is proportional to the charge weight W , then the crater dimensions will be proportional to $W^{1/3}$. This cube root scaling law, predicted by dimensional analysis on the basis of certain simplifying assumptions, has been widely used (see, e.g., Lampson, Reference 26, page 114).

An extensive study of craters from surface explosions and scaling laws, Vortman⁽⁴⁰⁾, indicated departures from the $W^{1/3}$ scaling. Much more data were available from buried charge explosions in earth and rock than from surface bursts, and, according to Vortman, the available experimental surface-burst data (from a variety of chemical and nuclear explosions) were occasionally contradictory. If empirical laws of the form

$$r_a = C_1 W^{n_1}, \quad d_a = C_2 W^{n_2}, \quad \bar{V}_a = C_3 W^{n_3} \quad (59)$$

are fitted to the data for apparent crater radius r_a , depth d_a , and volume \bar{V}_a , the data from nuclear and chemical explosions are consistent in indicating that n_1 is larger than one-third. Departures from cube-root scaling in large events are sometimes attributed to the importance of gravity forces. For surface bursts, however, departures from cube-root scaling have also been observed with small charges where the gravity forces are negligible compared to the material strength. The apparent crater data seem to require a value for n_2 different from n_1 , which would violate geometric similarity.

By contrast, more recent studies in the Mine Shaft series (24,41) have indicated that true crater dimensions for surface

explosions in rock scale fairly consistently for charge weights ranging over five orders of magnitude, but not by cube-root scaling. The best correlation was obtained by scaling the true crater dimensions by $W^{1/2.7}$ and the height of burst by $W^{1/3}$. Figure 15 shows true crater dimensions as a function of charge weight for true surface shots (dashed curves) and HOB = $0.9 r_c$ shots (solid curves), showing remarkable agreement with the $W^{1/2.7}$ scaling.

The 1974 Waterways Experiment Station compendium (Reference 11, p. 100 and pp. 132 to 135) presents graphs and tables including some of the same data in a different fashion. A best fit to eight rather scattered available data points for basalt and granite (based on two charge sizes) for scaled HOB between 0.05 and 0.20 ft/lb^{1/3} was represented by $r_t = 0.195 W^{0.418}$ and $d_t = 0.023 W^{0.518}$ while eight points (seven charge sizes) for scaled HOB between -0.05 and +0.05 ft/lb^{1/3} were well represented by $r_t = 1.211 W^{0.315}$ and $d_t = 0.588 W^{0.271}$. Crater dimensions are in feet for W in pounds of TNT. Hence the exponent $1/2.7 = 0.37$ suggested by Figure 15 is by no means universal.

For the purposes of the present study the two calibration series marked CCS in Figure 15 are more useful than the larger charges. The calibration series consisted of one-pound spherical charges on one-yard cubical blocks of cement grout and 1000-pound spherical charges in a natural granitic rock medium⁽⁴¹⁾. Figure 15 is taken from Reference 24 reporting on the Mine Ore event, two 100-ton spherical charges. The figure also includes data from two comparable series of previous true-surface-shot cratering tests. The Flat Top I event⁽⁴²⁾ had 20-ton TNT spheres in limestone. The Multiple Threat Cratering Experiment⁽⁴³⁾, marked MTCE in Figure 15, had 4000- and 16,000-pound TNT detonations in basalt, four of which were spherical charges in geometries comparable to those of Mine Ore.

The 19 one-pound calibration shots were especially interesting, since the cement grout had compressive strength and pulse velocity comparable to those of normal concrete. The average static compressive strength was about 4500 psi. Table 3 summarizes the properties of the grout. This series⁽⁴¹⁾ specifically studied the effect of varying the height of burst from HOB = 0 (half buried) to HOB = $2r_c$ with the results shown in Table 4. Consistency of the results is quite good except for shots 13 and 18.

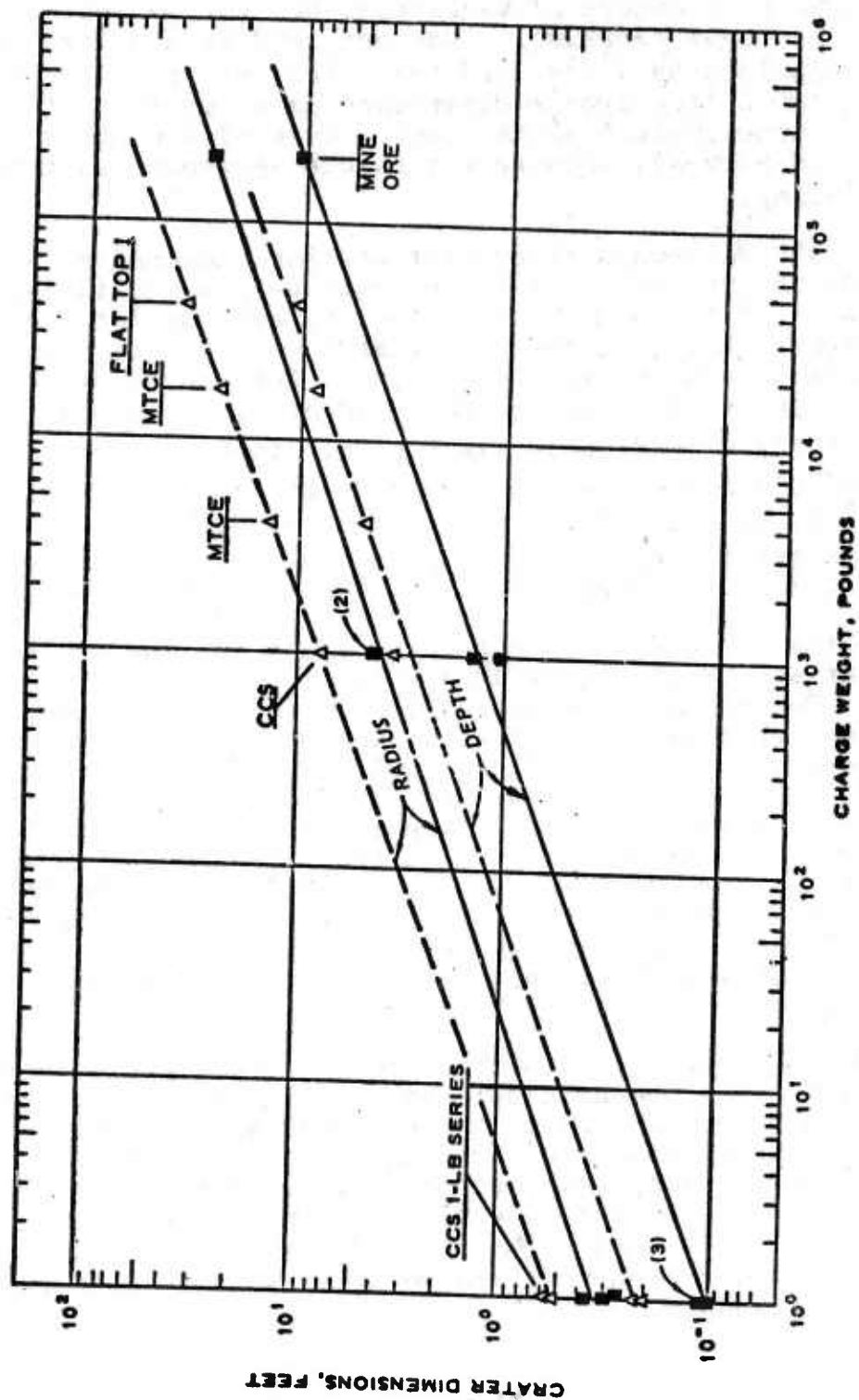


Figure 15. True Crater Dimensions as a Function of Charge Weight for True Surface (Dashed Curves) and $0.9r_c$ HOB (Solid Curves) Shot Geometries

The ten 1000-pound calibration shots⁽⁴¹⁾ (cast spheres of TNT) were fired over a granite medium at HOB ranging from $2r_c$ to $-0.3r_c$. For those events in which the bottom of the charge was below the rock surface ($HOB < 1.0r_c$), a charge emplacement hole was excavated roughly conforming to the charge shape. A layer of high-early-strength cement grout was plastered around the hole, shaped with a template to fit the charge, and allowed to harden. Hydrostone cement was finally used to provide intimate coupling from the charge to the granite. Nylon slings supported the charges for $HOB > 1.0r_c$. For the surface-tangent shot, the charge was merely placed on the surface and held in position with small wooden wedges.

Because of the natural jointing patterns in the granite the true craters were not as symmetrical as for the 1-pound shots in grout. Crater radii along a joint through ground zero (GZ) are considerably longer than those perpendicular to the joint. Some parts of the true crater boundaries were planes due to the jointing. Despite these facts, average true crater dimensions varied in a consistent fashion with HOB except for one shot. The combined results of the two calibration series and the comparable data (for the dependence of crater depth and crater radius on HOB) from the other experiments cited in Figure 15 are shown in Figures 16 and 17 (from Reference 24).

The upper Figure 16 plots true crater depth d_t in charge radii versus HOB also in charge radii (upper scale). This is equivalent to conventional cube root scaling. In the lower Figure 16 the same data are replotted with d_t scaled by $W^{1/2.7}$. Figure 17 shows a similar representation of the true crater radius $r_t W^{1/2.7}$ versus $HOB/W^{1/3}$. Davis⁽⁴¹⁾ commented as follows: "Since the position of the bottom of a spherical charge with respect to the medium surface is so critical for this range of HOB's, the HOB must still be scaled by $W^{1/3}$ in order to preserve the relation between the physical spacing of the charge center, the bottom of the charge, and the surface of the medium... In addition, the curve drawn through the data points (Figure 17) acquires an 'S' shaped bend where the HOB's are very close to the surface tangent geometry. This, of course, indicates that the cratering potential of an HE charge is much more sensitive to the position of the bottom of the charge with respect to the surface of the medium than to the position of the center of the charge."

The last sentence quoted was intended, of course, to apply only to the near surface range of HOB's. These observations also suggest the need for studying the effects of charge shapes other than spherical in order to draw practical conclusions

TABLE 3. PROPERTIES OF CEMENT GROUT

| Mixture Design Specifications ^a | | Results of Laboratory Tests on Cylinders ^b | | | |
|--|-------------|---|-------------------------|-----------------------------------|---|
| Material | % by Weight | Cylinder No. | Pulse Velocity (Ft/Sec) | Static Compressive Strength (Psi) | Dynamic Compressive Strength ^c (Psi) |
| Cement | 25 | 1 | 12,820 | 3,820 | -- |
| Water | 11 | 2 | 13,160 | 5,840 | -- |
| Sand | 62 | 3 | 12,820 | 4,040 | -- |
| Calcium chloride | 2 | 4 | 13,335 | 4,840 | -- |
| | | 5 | 12,660 | 3,860 | -- |
| | 100 | 6 | 12,985 | -- | 8,210 |
| | | 7 | 12,820 | -- | 6,430 |
| | | 8 | 12,985 | -- | 7,140 |
| | | 9 | 13,335 | -- | 8,750 |
| | | 10 | 12,820 | -- | 5,360 |
| Average | | | 12,974 | 4,480 | 7,178 |

- ^a Design strength at 28 days was 6,000 psi.
^b Cylinders were tested 10 days after pouring.
^c Load rise time was approximately 2 msec.

TABLE 4. TRUE CRATER DIMENSIONS

All charges were 1-pound TNT spheres with a radius (r_c) of 1.63 inches.

| Shot No. | Charge Position ^a HOB r_c | True Crater Depth d_t (Feet) | True Crater Radius, r_t | | | True Crater Volume v_t (In ³) |
|----------|--|--------------------------------------|---------------------------|-------------------|--------------------------------|---|
| | | | Maximum (Feet) | Minimum (Feet) | Average ^b (Feet) | |
| 1 | 0 | 0.23 | 0.74 | 0.59 | 0.68 | 240 |
| 2 | 0 | 0.23 | 0.74 | 0.61 | 0.65 | 200 |
| | | Avg 0.23 | Avg 0.74 | Avg 0.60 | Avg 0.67 | Avg 220 |
| 18 | 0.5 | 0.27 | 0.70 | 0.55 | 0.60 | -- |
| | | Avg 0.27 | Avg 0.70 | Avg 0.55 | Avg 0.60 | -- |
| 3 | 0.7 | 0.17 | 0.60 | 0.45 | 0.49 | 110 |
| 4 | 0.7 | 0.17 | 0.58 | 0.37 | 0.47 | 70 |
| 17 | 0.7 | 0.16 | 0.52 | 0.40 | 0.45 | -- |
| | | Avg 0.17 | Avg 0.57 | Avg 0.41 | Avg 0.47 | Avg 90 |
| 5 | 0.8 | 0.14 | 0.43 | 0.30 | 0.37 | 34 |
| 6 | 0.8 | 0.17 | 0.60 | 0.39 | 0.50 | -- |
| 16 | 0.8 | 0.11 | 0.47 | 0.33 | 0.39 | -- |
| | | Avg 0.14 | Avg 0.50 | Avg 0.34 | Avg 0.42 | Avg 34 |
| 7 | 0.9 | 0.09 | 0.48 | 0.26 | 0.38 | -- |
| 8 | 0.9 | 0.10 | 0.43 | 0.24 | 0.31 | 22 |
| 15 | 0.9 | 0.10 | 0.45 | 0.21 | 0.28 | -- |
| | | Avg 0.10 | Avg 0.45 | Avg 0.24 | Avg 0.32 | Avg 22 |
| 9 | 1.0 | 0.07 | 0.22 | 0.19 | 0.20 | -- |
| 10 | 1.0 | 0.09 | 0.22 | 0.19 | 0.21 | 7.8 |
| 14 | 1.0 | 0.08 | 0.21 | 0.13 | 0.17 | -- |
| | | Avg 0.08 | Avg 0.22 | Avg 0.17 | Avg 0.19 | Avg 7.8 |
| 13 | 1.1 | 0.09 | 0.68 | 0.47 | 0.57 | -- |
| | | Avg 0.09 | Avg 0.68 | Avg 0.47 | Avg 0.57 | Avg -- |
| 12 | 1.3 | 0.08 | 0.33 | 0.13 | 0.23 | -- |
| | | Avg 0.08 | Avg 0.33 | Avg 0.13 | Avg 0.23 | Avg -- |
| 11 | 1.5 | 0.07 | 0.32 | 0.15 | 0.24 | -- |
| | | Avg 0.07 | Avg 0.32 | Avg 0.15 | Avg 0.24 | Avg -- |
| 19 | 2.0 | c | c | c | c | c |

^aDistance from grout-air interface to center of gravity of charge.

^bAverage of eight radii at 45-degree intervals for Shots 1-10; average of four radii at 90-degree intervals for Shots 11-19.

cNo crater was formed.

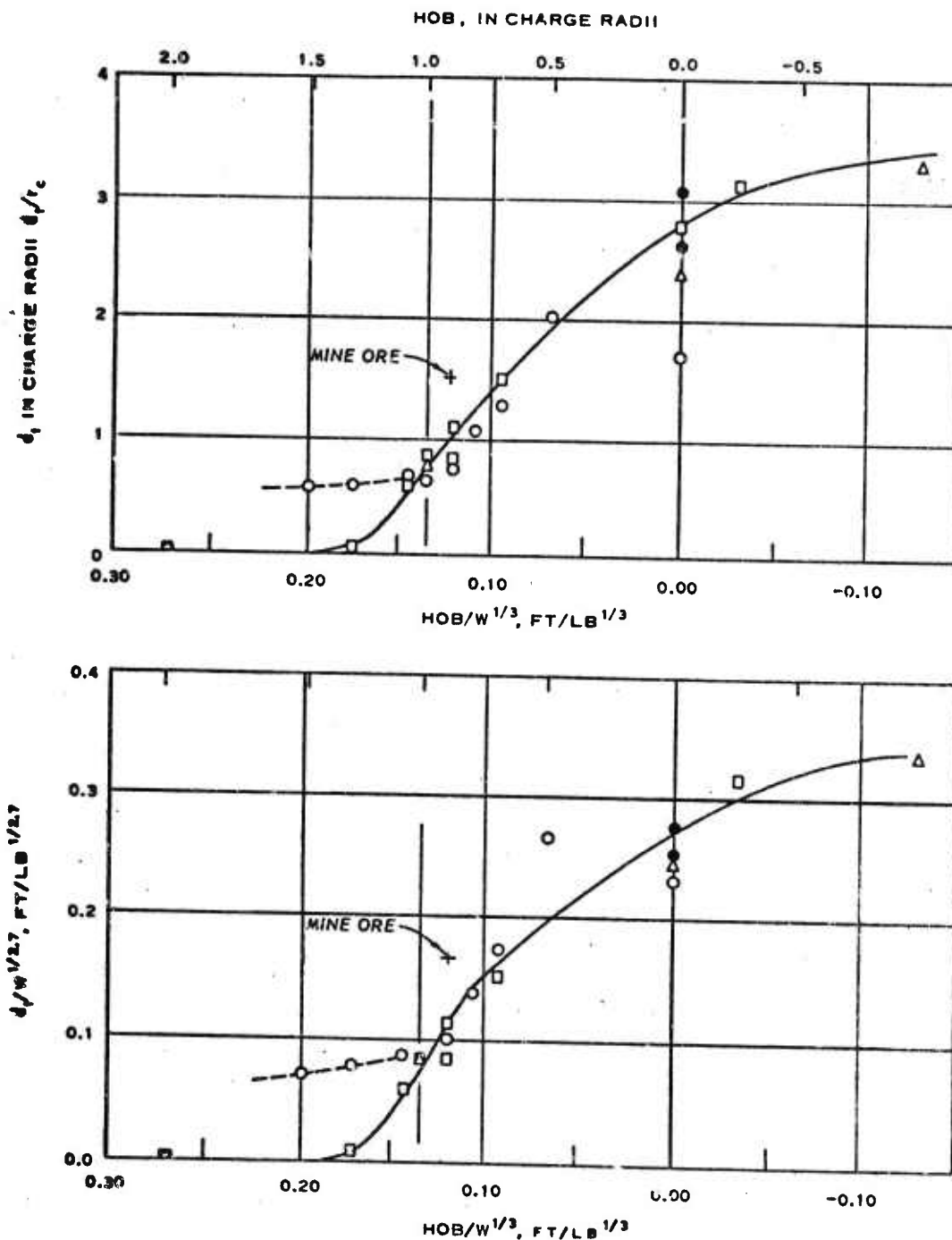


Figure 16. Comparison of Scaling True Crater Depth by $W^{1/27}$ as Opposed to Scaling by Charge Radii ($W^{1/3}$ Scaling), with a Constant $W^{1/3}$ Scaling Factor for Height of Burst

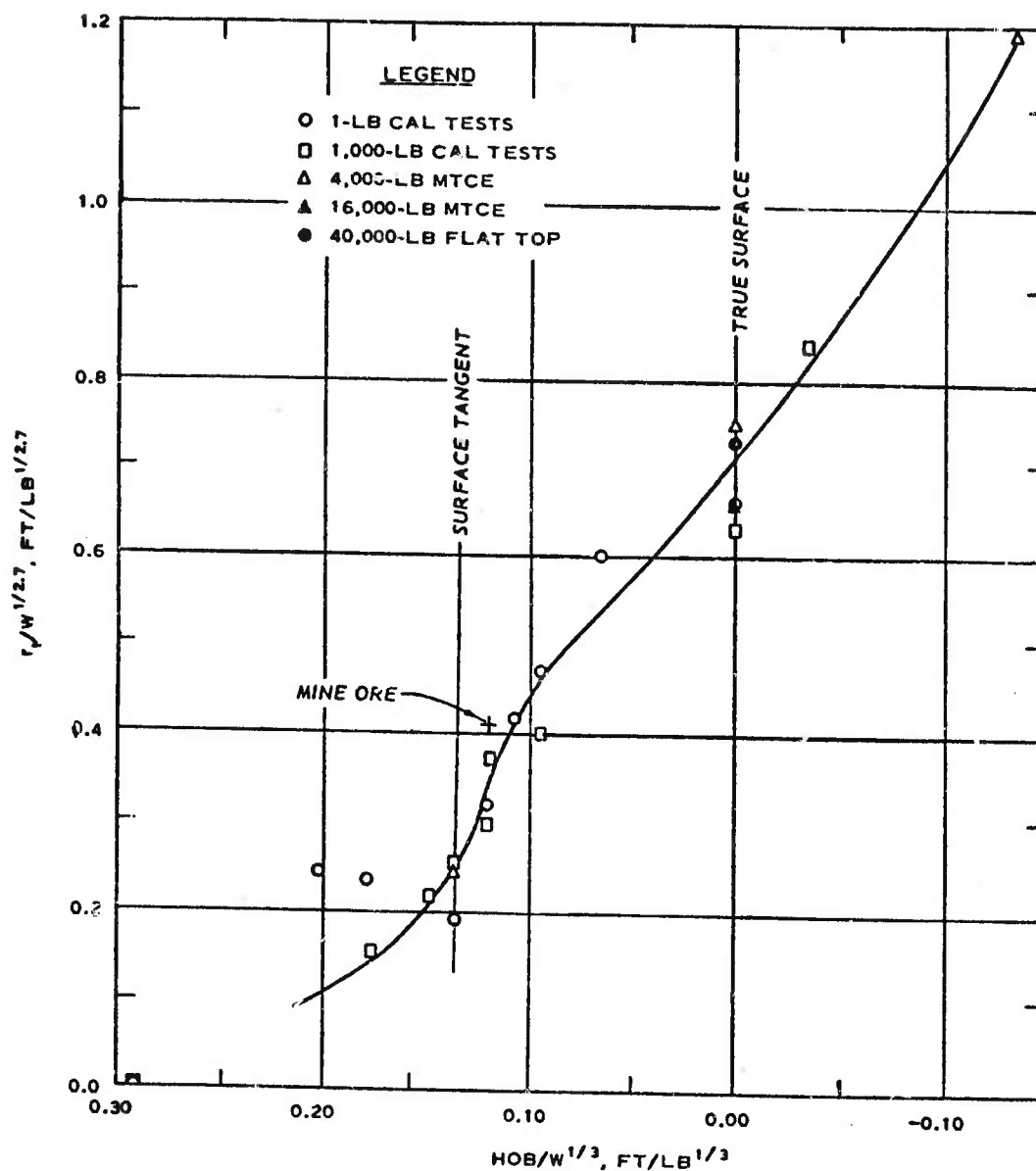


Figure 17. True Crater Radius, Scaled by $W^{1/2.7}$, as a Function of Height (or Depth) of Burst, Scaled by $W^{1/3}$ (Geometric Scaling), for Spherical TNT Charges Fired in Hard Rock

about cratering from surface bursts of HE. Nevertheless, the results presented establish the fact that cratering from surface bursts can be predicted reasonably well under controlled surface contact conditions.

Both Figure 16 and Figure 17 exhibit discrepancies between the scaled crater dimensions for the 1-pound charges and those for the 1000-pound charges in the HOB range above the surface tangent configuration. The craters formed from the 1-pound shots in this HOB range appeared to be spall craters resulting from airblast-induced shock stresses. Two possible explanations for the discrepancies were suggested: (1) the possible existence of still another scaling relation for these HOB's, or (2) that the unit strength (as opposed to en masse strength) of the granite was so much higher than that of the grout. Although the en masse strength of the granite is usually low due to joints, cracks, weathering, etc., care was taken in the selection of the calibration series test areas to provide competent, unweathered rock bodies for testing. Thus, the smaller craters formed by airblast-induced stresses in the 1000-pound shots may simply be a result of higher medium strength.

Evidently what is needed to develop empirical formulas for concrete is a series of controlled model studies all in concrete. The properties of the concrete could be known more accurately than those in the field tests over granite. Small-scale tests, e.g., with charge masses in the ratios 1:8:27, could be used for studies of charge shape and placement and some assessment of the scale effects. A follow-up program should then check on extending the model to larger charges (and more costly experiments). Extrapolation is a much more risky estimation procedure than interpolation.

It has been suggested⁽⁴⁴⁾ that the complex behavior of concrete does not lend itself to scaling procedures. One possible reason for the suggestion is that concrete exhibits rate dependence. The modulus of elasticity can increase by 50 percent and the ultimate strength by 30 to 80 percent as the strain rate increases from about 10^{-3} to 10^3 sec⁻¹. Nevertheless, in view of the success of scaling in soils and in rock media that are at least as complex as concrete in their behavior, there is a probability of reasonable success with a moderate effort.

The following section will survey briefly some approaches to the prediction of dynamic deformation, penetration, and cratering in concrete that are of a more fundamental character than the empirical scaling formulas.

3.3 More Fundamental Approaches

3.3-1 Introduction

When the entire range of effects on finite concrete blocks and slabs (including penetration by shaped charges followed by explosive cratering, spall and corner fractures) is to be treated, a complete analysis may be needed of some typical cases in order to establish practical guidelines. This section sketches the state-of-the-art as revealed by the literature survey and laboratory visits. A great deal has already been accomplished in this difficult area, but much more fundamental research is needed before it will be possible to prescribe a specific series of computer simulations of surface and near surface shots (including penetration cases) which would be reasonably certain to furnish a set of tables or curves that could be used for practical damage estimation (something comparable, for example to the Lawrence Livermore Laboratory's Aids for Estimating Effects of Underground Nuclear Explosions(45)).

The fundamental studies involve three interrelated types of investigation:

1. Computational (Code development)
2. Theoretical (Constitutive equation formulation)
3. Experimental (Determination of properties and verification of predictions).

Code development is continuing at a rapid pace, but it has already outstripped the other areas. There are in existence several one- and two-dimensional codes capable of making useful analyses of the problems if sufficiently good characterization of the material response and of the contact conditions can be made. The code developments will not be summarized at length, since they are quite well known. A recent book(46) includes chapters surveying characteristics methods as well as Eulerian, Lagrangian, and Particle in Cell numerical methods. There are many one-dimensional codes. Many of the two-dimensional Lagrangian calculations are done with either HEMP(47) or TOODY(48), both of which use difference equations developed by Wilkins(47). TENSOR(49), an earlier Lagrangian code, has been used for many nuclear cratering calculations(32).

Read and Maiden(50) surveyed the current knowledge in 1971 on the dynamic behavior of concrete. At the higher stress levels the most extensive experimental wave propagation data then

available was by Gregson(51), who used a gas gun to determine uniaxial strain response of thin plate specimens to flyer plate impacts (stresses from 40,000 psi to 8,000,000 psi) and attempted to define the shock Hugoniot. Below 360,000 psi a two-wave structure was confirmed and a relatively dispersive elastic precursor was observed. Read and Maiden compared calculations based on two constitutive models (a simple elastic-plastic model and a porous medium model) with Gregson's experimental results; neither gave good agreement. They concluded that additional experiments are needed to characterize the Hugoniot in the 0 to 720,000 psi range which is of the greatest practical importance. Moreover, since there was a complete absence of data on attenuation of thin stress pulses, they concluded that systematic studies of release wave propagation and attenuation are required before a realistic constitutive model can be developed.

The situation appears not to have changed much since 1971. There is still a lack of the kind of experimental data needed to characterize even the uniaxial strain response of concrete to short duration pulses, despite the great importance of such information in the area of defense analysis and design.

Approximately uniaxial strain conditions prevail in blast loadings that act over a large surface area and also in the loading spherical wave front at large distances from a point charge. Because the equipment and expertise for the uniaxial strain experimentation (either by gas gun or explosively driven flyer plates) are so well developed, it should be used to obtain the needed data for a number of well-defined concrete materials.

For application to near-surface shot explosive loading and penetration problems it will be necessary to go beyond the uniaxial strain studies. The next step will be to consider spherical waves. Because of the divergent nature of the waves there is less tendency to shock up and consequently greater effect of material shear strength than in the uniaxial case. Spherical wave studies would give important additional information about the kind of material response that governs a significant part of the penetration behavior and also the response to surface contact explosive loading over a small area. These applications do not have spherical symmetry but, at best, axial symmetry.

Three configurations for experimental and analytical research may be distinguished:

- (1) Uniaxial strain waves
- (2) Spherical waves
- (3) Axially symmetric problems.

A great deal of work has been done in the first configuration with other materials but very little with concrete. The spherically symmetric case has recently been the subject of some studies in cement grout, primarily for testing in material gage recording techniques to be used later in rock media. The axially symmetric case presents additional problems both experimentally and computationally. It involves two space dimensions, greatly increasing the number of experimental recording positions needed to describe the wave, and it admits shear cleavages or sliding surfaces that complicate the computation. The axially symmetric geometry will eventually have to be treated for practical applications, but it would seem more profitable at this stage of knowledge to pursue the spherical case first. Section 3.3-2 discusses some approaches to this case that have been made or proposed. Then Section 3.3-3 considers constitutive equations.

3.3-2 Spherical Wave Experiments

R. P. Swift⁽⁵²⁾ of Physics International has proposed an experimental procedure for spherical wave loading of large concrete blocks by buried charges, using in-material piezoresistive stress gages and/or electromagnetic particle-velocity gages to record the wave. Figure 18 shows one of the several configurations that Swift suggested. By placing the explosive sphere off-center in the block, the response at several different radii can be monitored. Physics International has applied the technique to a variety of geologic media, including granite⁽⁵³⁾, tuff, basalt, clay, and sandstone⁽⁵⁴⁾. Application to concrete would be straightforward and would yield important information if the concrete mix, cure, etc., are well defined and controlled. Figures 19 and 20 show some of the records in granite and sandstone. The particle velocity gages are believed to be somewhat better than the stress gages, but both are good enough to provide useful results.

At Stanford Research Institute a preliminary program used concrete blocks for testing in-material gage measurement techniques for later use in soft rock⁽⁵⁵⁾. Concrete was selected because it provided an inexpensive and convenient experimental medium. Figure 21 shows the test geometry. The liquid explosive (nitromethane) was introduced into the aluminum sphere through the 2-inch access tube about 15 minutes before the shot.

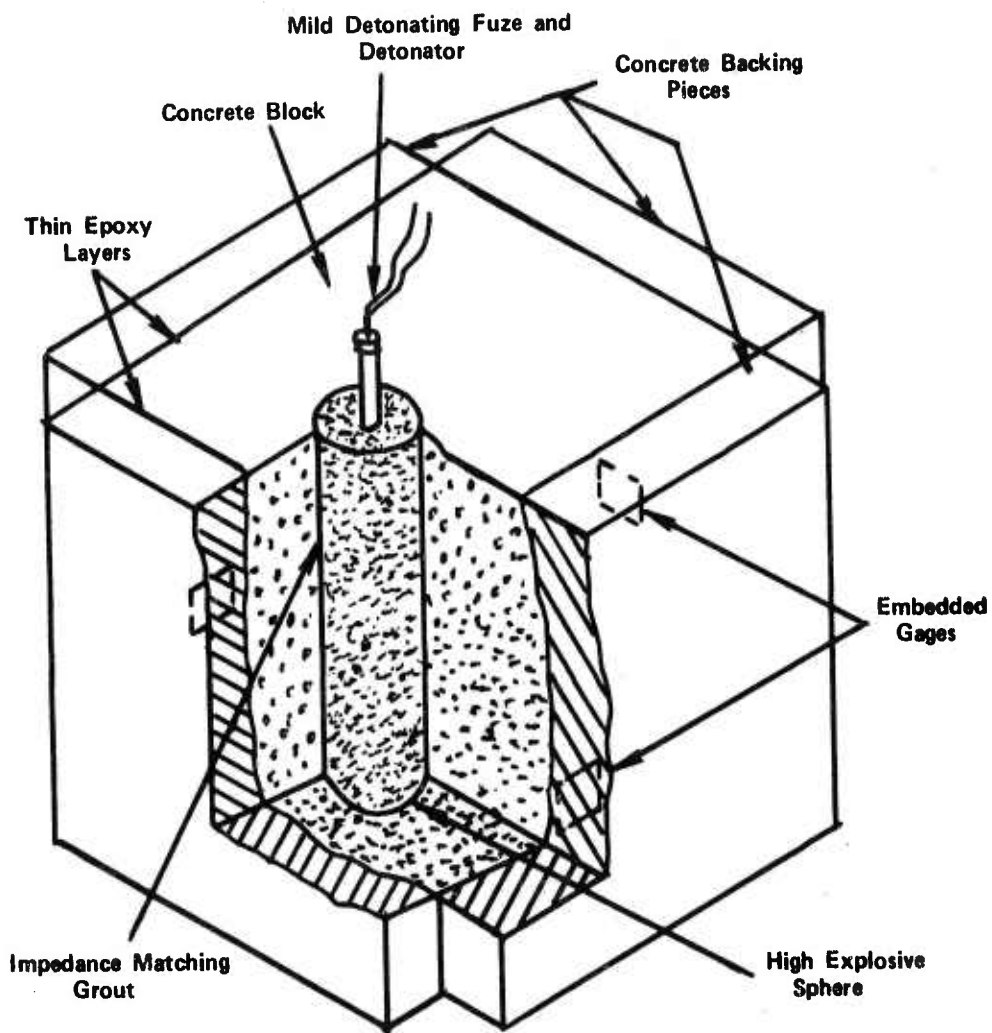


Figure 18. Experimental Configuration for Measuring Spherical Stress Wave Response at Different Radii

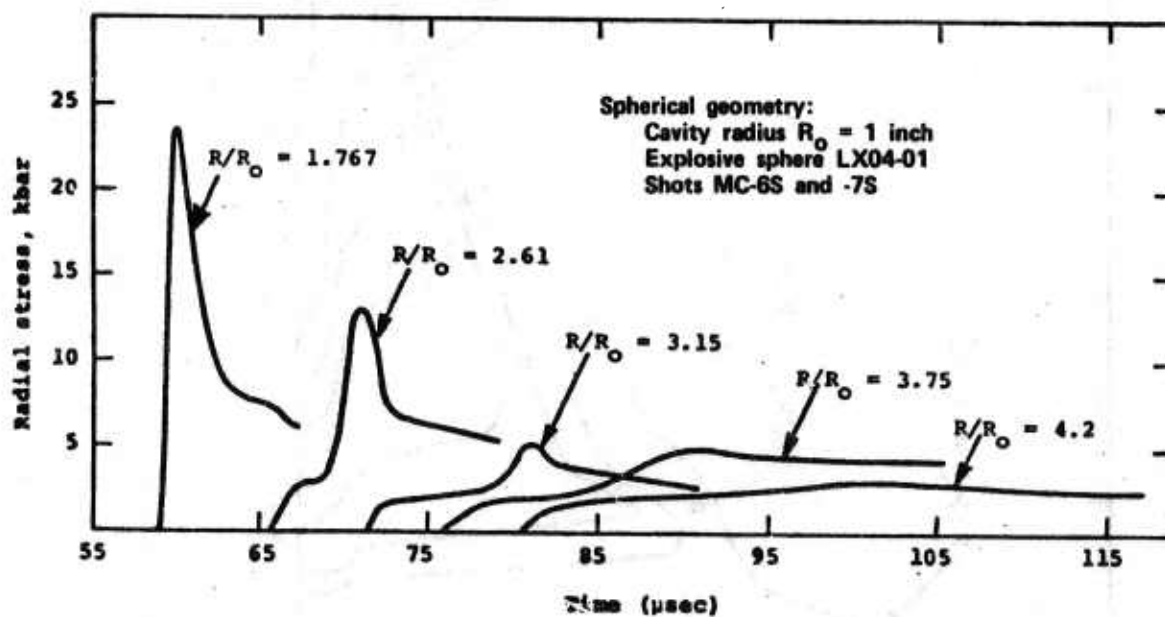
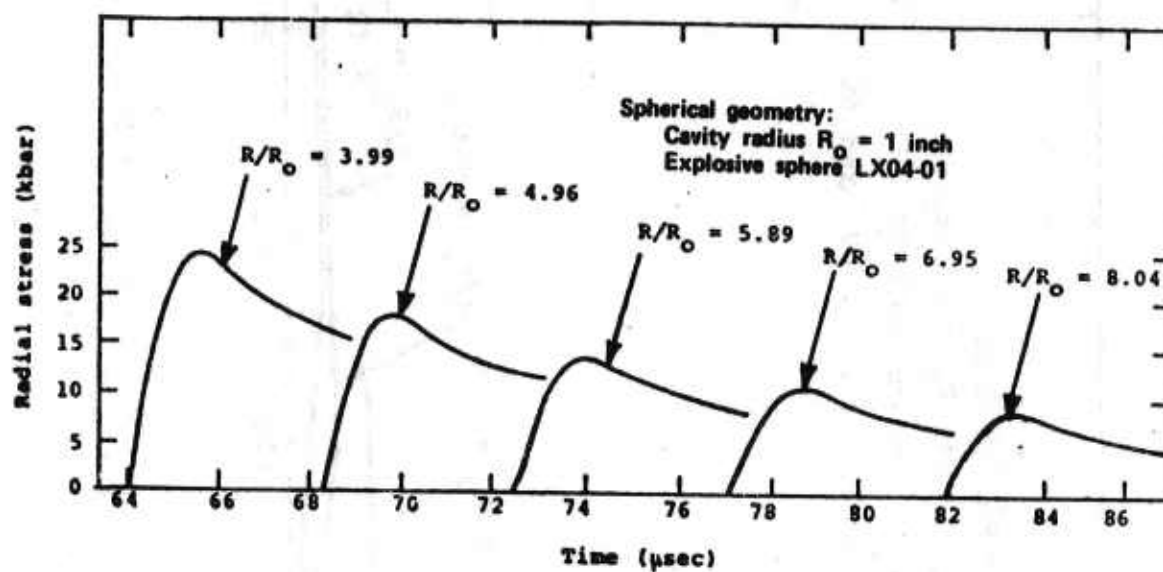


Figure 19. Experimental Radial Stress-Time Histories for Spherical Waves in Various Geological Materials

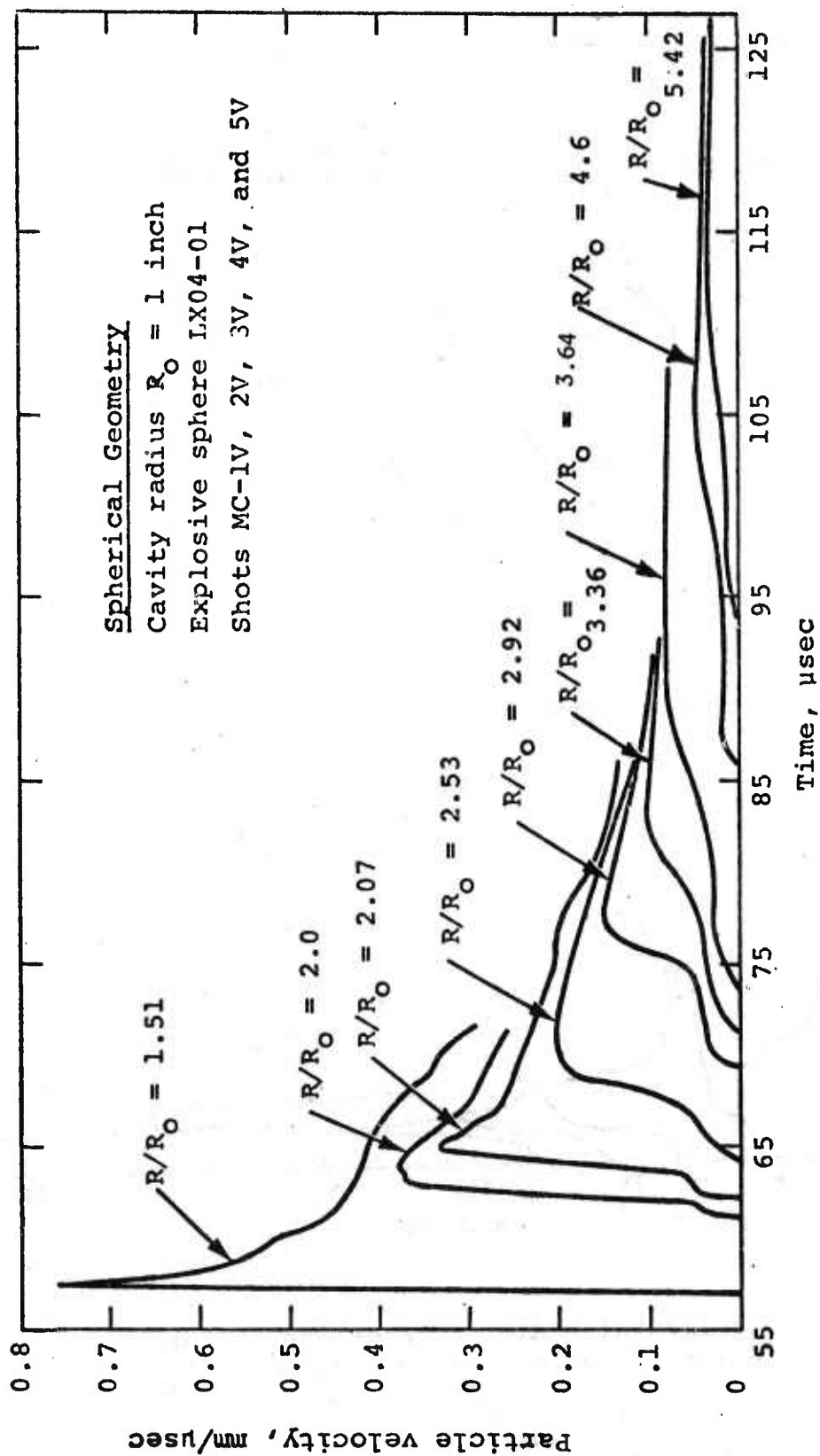


Figure 20. Experimental Particle Velocity-Time Histories for Dry Sandstone Based on Physics International MIXED COMPANY Experiment (54)

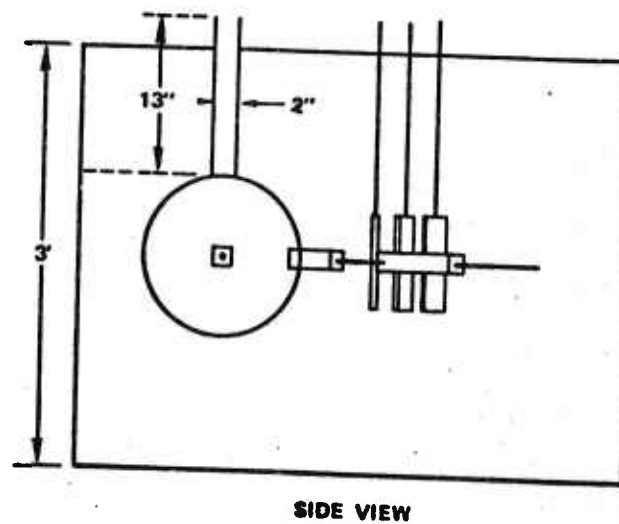
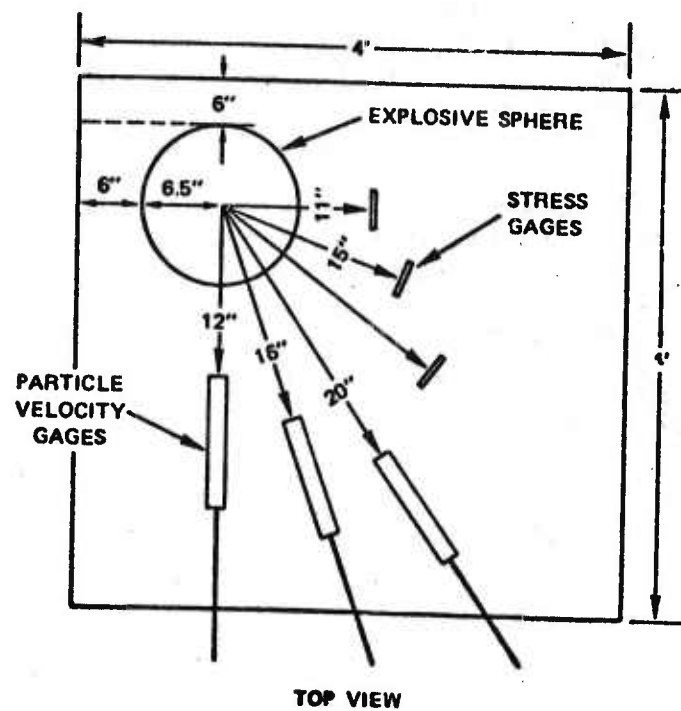


Figure 21. Top and Side View of Concrete Block Assembly
(Gage Geometry in this Drawing Corresponds to Experiment
11-A of Reference 55.)

The particle velocity gages were of a different type (mutual inductance gages, introduced by Engineering Physics Company⁽⁵⁶⁾ and adaptable for use in the field). Figure 21 shows an assembly with three stress gages and three velocity gages. Six blocks were tested in the series reported in Reference 56.

Some of the gages were actually cast into the material, while others were inserted into holes that were then filled with grout. In all six experiments, concrete cure was about two weeks. Drill hole gages were installed seven days after the pour, and the grout in the holes cured for about a week before the shot. Considerable difference was noted between the in-material gages and the grouted gages in the measured impulse. The stress from the in-material gages decayed shortly after the peak (e.g., 20 to 30 microseconds) but remained large for the grouted gages for 100 to 200 microseconds. There was some difference in the grout mix and that of the parent concrete, and possibly the surrounding porous concrete drew moisture out of the grout during its cure. Possibly a better matching grout can be found, but the experiments show the necessity for careful validation of any proposed in-material gage technique.

With metals and some other materials in hypervelocity impacts a considerable amount of information is obtainable by measurements of back-face velocities and stresses by various techniques on specimens of different thicknesses. Classic techniques using fly-off pellets of the same material as the specimen can be used, and should in particular be advantageous in validating the results from in-material gages.

Prater⁽⁵⁷⁾ has used a target whose basic configuration is a half cylinder impacted normally at the center of the flat face. When the cylinder radii became large enough so that peak stresses fell below values where the target strength could be ignored (i.e., below the hydrodynamic shock-wave region), the shape of the target was changed so that the curved surface was replaced by several flat surfaces each perpendicular to the radius drawn from the impact point and all at the same distance. Fly-off pellets were mounted on these surfaces as well as piezoelectric pressure sensors. A modified larger concrete version of such a target, loaded by a surface explosive, could be used to measure the waves emanating from the crushed and cratered region near the loaded face. This gives a situation more like the surface shots considered in preceding parts of this section than the spherical wave geometries. Apparently no such experiments have been made or proposed to be made in concrete, but they appear to be feasible. Preliminary experiments without in-material gages, using only the fly-off pellets, would be very easy to perform. With the preliminary results available to

guide experimental design it might be worthwhile to use in-material stress and/or velocity gages in a subsequent series of tests.

Section 3.3-3 considers the formulation of constitutive equations.

3.3-3 Constitutive Equations

In the immediate vicinity of the explosively loaded area, during the loading phase, the hydrostatic pressure is so large that the pressure-volume equation of state governs and material strength parameters are negligible. The study of many other solids in this hydrodynamic regime is well advanced. For surveys see References 46, 58 and 59. As Read and Maiden⁽⁵⁰⁾ pointed out, however, the needed data on concrete is still not available.

In the unloading phase, even for the regions adequately described by the hydrodynamic theory during loading, the situation is more complicated. Because of attenuation by overtaking rarefaction waves and spherical divergence, shock-wave amplitudes quickly drop to levels where material strength properties are important. The dynamic strength properties cannot be adequately measured in laboratory experiments with homogeneous stress states, but must be determined in situations where wave propagation is occurring. As a result, these properties are largely unknown for most materials and certainly unknown for concrete.

Various kinds of constitutive equations have been postulated, with some unknown parameters characterizing the material properties. Predicted wave propagation response for specific cases is then compared with experimental records. The computations can be made with assumed values of the parameters and then repeated with more-or-less sophisticated parameter identification techniques⁽⁶⁰⁾, adjusting the parameters to get a best fit to the experiments. This iterative procedure can become very expensive when each iteration involves a large computer solution of a wave-propagation problem. Lagrangian analysis based on multiple in-material gage records^(61,62,63) may avoid the iterations. One version of this will be discussed briefly in Section 3.3-4. Some of the constitutive formulations which have been proposed are discussed in the following paragraphs.

A 1971 survey⁽⁶⁴⁾ listed four inviscid and isothermal mathematical models for geologic materials, representing the then current state of the art: (1) an ideal elastic-plastic material

model with different constants in loading and unloading; (2) a variable moduli material with different material constants in loading and unloading; (3) a capped elastic-plastic material for soils in which the cap on the yield condition is made a function of the plastic volumetric strain; and (4) a capped elastic-plastic model for rock in which the cap is a function of a strain parameter (strain hardening). The advanced elastic-plastic material models were developed from the Drucker-Prager soil mechanics model, with deviatoric yield stress a function of the mean stress. This led to a nonlinear yield envelope in stress space, whose normal had a component such that (by the associated flow rule) a volume increase or dilatancy always accompanied shear deformation. These models can approximate much of the experimental data and are the easiest to fit, but they cannot match standard triaxial tests, which lead to compaction instead of dilatation.

The variable moduli equations resemble differentiated isotropic elastic equations: $\dot{S}_{ij} = G\dot{\epsilon}_{ij}$ for the deviators and $\dot{p} = K\dot{\epsilon}_{kk}$ for volume, but G and K are functions of the dilatation (or of the pressure) and G may also depend on the deviatoric stress invariants, with different dependences in loading and unloading. The variable moduli models are relatively easy to fit and have given the best fit to most of the data available. Because they do not incorporate a yield transition, they are simple to use in a computer program. As in deformation theories of plasticity their use is appropriate only for proportional or near proportional loading. They can be used for spherically symmetric waves.

The cap models represent a further development of the advanced elastic-plastic models, closing the yield surface on the compression side with a cap whose normal direction (over most or possibly all of the cap) leads to compaction instead of dilatation. An indirect approach is required to fit experimental data. Most applications so far appear to have assumed an elliptic shape for the cap in the $J_1, \sqrt{J_2}$ - plane. (J_1 is the first invariant of the stress and J_2 is the second invariant of the stress deviator). The elliptic cap has been taken with center on the J_1 axis and with horizontal and vertical semiaxes in a constant ratio. Further requirement as to how it meets the yield envelope (e.g., tangent) then leaves only one parameter to fit to hardening data. The selection of the elliptic shape for the cap is purely arbitrary, but it was reasonably simple to fit and seemed to give the right kind of shape. A more general shape could be used, depending on more than one hardening parameter. The cap models appear to be capable of matching all the standard test data and much of the wave propagation data.

The models discussed above are all rate independent. Experimental evidence suggests that material response is rate dependent. The models are fitted when possible from experimental data corresponding to loading rates comparable to those in the problem of interest. Viscoplastic models can also be developed when enough data is available. The most primitive version of an elastic-plastic material was one of the two constitutive equations used by Read and Maiden⁽⁶⁰⁾ to try to model the dynamic uniaxial strain data of Gregson⁽⁶¹⁾ for concrete. This model assumed no hardening and no plastic volume change and gave poor agreement with the experimental results. The other model used was a porous medium model, which also gave poor agreement. S. J. Green, et al, at Terra Tek, Inc. have recently completed a program⁽⁶⁵⁾ investigating the low strain rate and moderate stress level of behavior of concrete, including a systematic experimental study of hydrostatic and multiaxial stress behavior. More advanced elastic-plastic models than those used by Read and Maiden, including the cap models, have been more successful in rock media⁽⁶⁴⁾ and should also be suitable for concrete. Although it appears that concrete data have not yet actually been fitted to any of these advanced elastic-plastic or cap models, Swift⁽⁵²⁾ in 1972 suggested a cap model as appropriate for modeling the data he proposed to obtain from spherical wave experiments.

It is known that rock and concrete both flow when subjected to deviatoric stresses under high hydrostatic pressures. Thus, plastic models for these materials, usually considered brittle, are not unreasonable under high hydrostatic pressures. Near the surface of the target and in the later stages of unloading, where cracks and voids begin to open up, these models might not seem so appropriate. Nevertheless they have been used in soils and rock media with some success.

A different approach to modeling both ductile and brittle fracture in metals under hypervelocity impact has been used by Stanford Research Institute^(66,67). It has been observed that in the incipient fracture phase of the deformation (e.g., back-face spall of a thin plate) where voids (in ductile materials) or cracks (in brittle material) form and grow, propagate and coalesce, the usual assumptions about metals no longer hold. The behavior of metals in this regime is not unlike that of granular soils or fracturing rock, exhibiting dilatancy, for example, and other types of behavior not usually associated with metals. They have modeled this regime in metals, both under uniaxial plate slap loading leading to back-face spall and under hypervelocity impact of a steel plate by a nylon sphere⁽⁶⁸⁾, the last using sophisticated two-dimensional computations, giving remarkable agreement with experiments. The nylon

sphere impact led to cratering, subcrater fractures, a phase-change zone, and back surface fractures.

The modeling of the nucleation and growth of the voids or cracks as rate processes is described in References 66 and 67. Modifications to the procedure used there for Armco Iron are described in Reference 69. One modification was to assume the nucleation of an exponential distribution of crack sizes at each time step. The form assumed for the distribution was considered reasonable in light of actual measurements in rocks^(70,71). This modeling technique could also be applied to penetration and explosive loading of concrete. It appears to be the most advanced modeling technique available. A major research program might lead to the design of a set of computer simulations, with experimental input of data and some verifications of predictions, that would permit construction of a set of graphs and tables for design guidance.

3.3-4 Lagrangian Analysis

In the introduction three interrelated types of investigation were identified: computational, theoretical and experimental. The interaction of the three is most evident in the relatively new approach based on multiple in-material gage records^(61,62,63) which is known as Lagrangian analysis. This approach was originally developed for plane waves, but has been extended to spherical symmetry. It involves multiple gage measurements of both stress and particle velocity at stations inside the medium, and subsequent direct deduction of the operative constitutive relation without iterative computations. The version of this method that is being developed at Stanford Research Institute^(72,55) does not make use of the two different phase velocities (one for stress and one for particle velocity) used in previous methods⁽⁶³⁾.

To illustrate the ideas, consider a spherically symmetric wave propagation. The Lagrangian (initial) and Eulerian radial distances are denoted by h and r , respectively. Initial and current densities are ρ_0 and ρ . Radial particle velocity and stresses are u_r and σ_r , while $\phi = \sigma_r - \sigma_\theta$ denotes the difference between radial and tangential stress. (For spherical symmetry the value of ϕ characterizes the deviatoric stress.) The conservation laws of mass and momentum and the definition of particle velocity furnish three equations:

$$\frac{\rho_0}{\rho} = \frac{r^2}{h^2} \left(\frac{\partial r}{\partial h} \right)_t, \quad (60)$$

$$\rho \left(\frac{\partial u_r}{\partial t} \right)_h = \left(\frac{\partial \sigma_r}{\partial r} \right)_t + 2 \frac{\phi}{r}, \quad (61)$$

$$u_r = \left(\frac{\partial r}{\partial t} \right)_h \quad (62)$$

among the five unknown functions (ρ , u_r , σ_r , r and ϕ) of the two independent variables h and t . This system is incomplete because it lacks the (unknown) constitutive equations.

From the multiple in-material gage data, portions of the solution surfaces $\sigma_r = \sigma_r(h, t)$ and $u_r = u_r(h, t)$ are constructed numerically (Figure 22).

The known equations furnish

$$r(h, t) = h + \int_{t_0}^t u_r dt \quad (63)$$

$$\epsilon_v(h, t) = \epsilon_v(h, t_0) - \frac{1}{h^2} \int_{t_0}^t \left[\frac{\partial}{\partial h} (r^2 u_r) \right]_t dt \quad (64)$$

where $\epsilon_v = 1 - (\rho_0/\rho)$ is volume strain, and

$$\phi = \rho \frac{r}{2} \left[\left(\frac{\partial u_r}{\partial t} \right)_h - \frac{r^2}{h^2} \frac{1}{\rho_0} \left(\frac{\partial \sigma_r}{\partial h} \right)_t \right] \quad (65)$$

The time derivatives needed in Equations (64) and (65) can be evaluated directly from gage profiles, but the spatial derivatives require evaluation of directional derivatives along suitable paths $\xi(t)$ in Figure 22 (e.g., paths parallel to the shock-wave front). The analysis then gives values of the remaining unknown functions of h and t , from which various stress-strain histories can be constructed. Suitable assumed forms for the constitutive equations are then fitted to this data. Note that iterated computations over the whole field are not required to determine the parameters in the assumed constitutive equations.

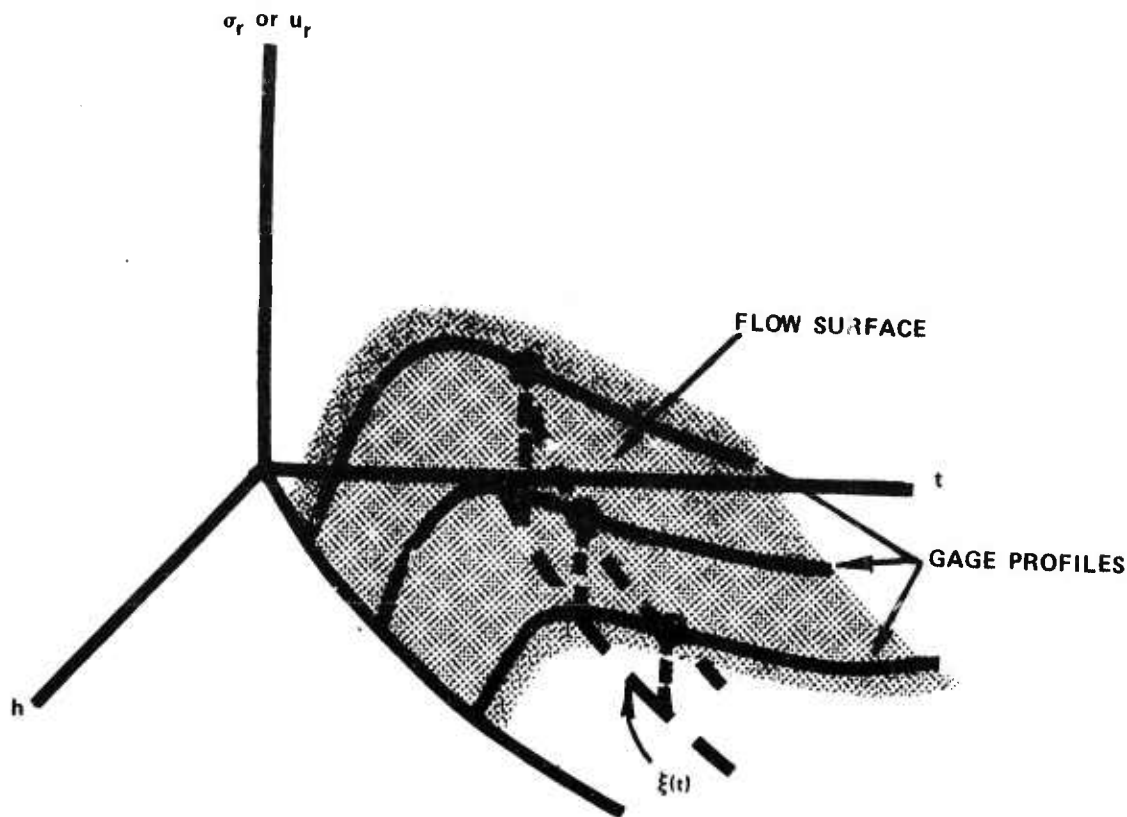


Figure 22. Stress or Particle Velocity Histories from Multiple Gages are Combined to Form a Surface in the Space-Time Plane

It may be noted from Equation (65) that in experimental profiles where the stress and particle velocity derivatives are large compared to their difference (e.g., in the rapid loading region) it will be difficult to determine ϕ accurately. The flow field in this region is also insensitive to the choice of the constitutive equation for the deviatoric stress. In the unloading regions, where the derivatives are smaller, the flow is more sensitive to the deviatoric stress, and the analysis provides better values for ϕ where ϕ is more important.

The SRI group has applied this procedure to laboratory experimental spherical wave data obtained by Swift of Physics International in blocks of Westerly granite⁽⁵³⁾ and of sandstone⁽⁵⁴⁾ with some success. The procedure is being developed for in situ studies of rock media sponsored by the Defense Nuclear Agency^(72,55). For such in situ field measurements, with gages grouted into boreholes in large expanses of rock media, the procedure will be subject to some uncertainties,

both from the individual measurement difficulties and from inhomogeneity. Much less uncertainty would be associated with the application of the method to studies in concrete under controlled conditions.

For spherically symmetric waves a variable moduli constitutive equation is easy to determine by this method, but for later use in two-dimensional geometries with nonproportional loading, a capped elastic-plastic (or possibly viscoplastic) model is more appropriate. For the tensile fracture regions more sophisticated rate-process void and crack nucleation and growth models like those that have been used for hypervelocity impact on metal plates(66,69) may be needed. The use of Lagrangian analysis for any of these is limited mainly by the difficulty of obtaining good experimental in-material gage data in the regions of interest.

3.4 Experimental Laboratory Study of Dynamic Tensile Fracture of Concrete Bars

3.4-1 Introduction

Because concrete is so weak in tension, spall and corner fractures may occur in the low-stress elastic regions far from the high-deformation cratering region of Figure 14 (Section 3.0). Since such damage in protective or containment structures is caused by wave propagation through the impacted medium and governed by the dynamic tensile strength of the material, information on the dynamic tensile fracture properties of concrete is needed.

At the present time, only a limited amount of data on the dynamic properties of concrete is available. This makes it difficult to use sound engineering judgment in the design of protective and containment structures. For example, in design of such structures to resist impact and blast loadings, the design dynamic tensile strength is arbitrarily selected as twice the static ultimate tensile strength(73). Some additional studies related to the dynamic impact properties of concrete have been reported in Reference 74. Results from those studies indicated that the compressive strength of concrete increased with the rate of loading, being about twice the static value at an intermediate strain rate of 10 in/in/sec. Furthermore, the dynamic elastic modulus was found to be approximately 1.5 times the static value, and the impact resistance of the material was found to increase with rate of loading. Some additional tests on the static and dynamic behavior of concrete have been reported in References 75 and 76. These studies,

conducted on impacted laboratory-scaled long bar specimens, of varying cure time and properties, have shown that the wave propagation velocity is similar to that of igneous rocks, that the dynamic elastic modulus is considerably greater than its static value, and that pulses of short duration and high rise time propagate with little dispersion and some attenuation depending upon the indicated strain level. Recent studies⁽⁷³⁾ indicate that a fracture strain energy criterion may provide a meaningful criterion for design against spall and corner fracture phenomena. In addition, some recent data reported on brittle materials other than concrete⁽⁷⁷⁾ indicate that a statistical correlation between static tensile fracture and compressive pulse fracture in long bar specimens may be possible.

At the back-face of a flat slab, the arriving compressive wave may be approximately a plane wave of uniaxial strain, which is reflected at a free back surface as a tensile wave, leading to tensile fracture under conditions of approximately uniaxial strain. Corner fractures occur under more complicated combined-stress conditions, but in the low-stress elastic regimes brittle fracture is often assumed to be governed by the maximum tensile stress and to be independent of the other stresses. The range of stresses and rates for which this maximum-stress failure criterion is valid has not been established. In the range for which it is valid, strength determination by bar tests, which are relatively easy to perform, should be useful.

In such tests an impulsive axial load is applied to the end of a long bar by a longitudinal impact. The compressive wave arriving at the far end is approximately a plane wave of uniaxial stress, which is reflected as a tensile wave. This reflected tensile wave is superposed on the oncoming compressive pulse. For exactly square waves and perfect reflection, the superposed waves would give zero stress for some distance from the reflecting end, until the tail of the oncoming compressive wave arrived, when a sharp tensile loading would produce fracture. In general the pulses are not square, and the excess of the tensile wave over the compressive wave builds up gradually until it exceeds the dynamic tensile strength at some section of the bar.

In the present investigation, information on the threshold tensile fracture stress of concrete bar specimens has been sought. Included in the results are data on the static tensile and compressive strength, and the influence of the geometrical size effects on impact fracture characterization.

3.4-2 Specimen Preparation

Long bar cylindrical specimens were prepared from high-early-strength cement (Portland III). Specimen composition and static properties are shown in Tables 5 and 6. The aggregates A-3 and A-4, supplied by NL Industries of Edgar, Florida, had the properties shown in Table 6. (D_{50} is the mean diameter of the sieve size that passes 50 percent of the sample. The uniformity ratio is $C_u = D_{60}/D_{10}$.)

Concrete was mixed in quantities sufficient to produce static tensile and compressive test specimens as well as the long dynamic tensile fracture specimens. Nominal dimensions of the bar specimens used in the test program were 0.75 and 1.5 inches in diameter by 18 inches long. Some photographs of typical specimens used for the static tension-compression tests as well as the long-bar specimens used in the dynamic impact studies are shown in Figures 23 and 24.

PVC tubes were used as molds for fabricating the cylindrical bar specimens. Spraying the interior surface with a mold release agent insured a smooth surface. For casting the specimens, the PVC tubes were held in a vertical position in a special jig fixture with the lower end sealed with a rubber stopper. The concrete mixture was added in 2-inch layers and consolidated by tamping. A second stopper was then used to seal the top end of the tube and the sides of the split PVC tubing sealed with waterproof tape. During the initial setting period, the tubes were placed in a horizontal position and allowed to set for three days in a moist cure environment. The samples were then moist-cured for an additional period of four days at which time the specimens were removed from the holds and air dried in a low humidity room.

3.4-3. Test Procedure and Results

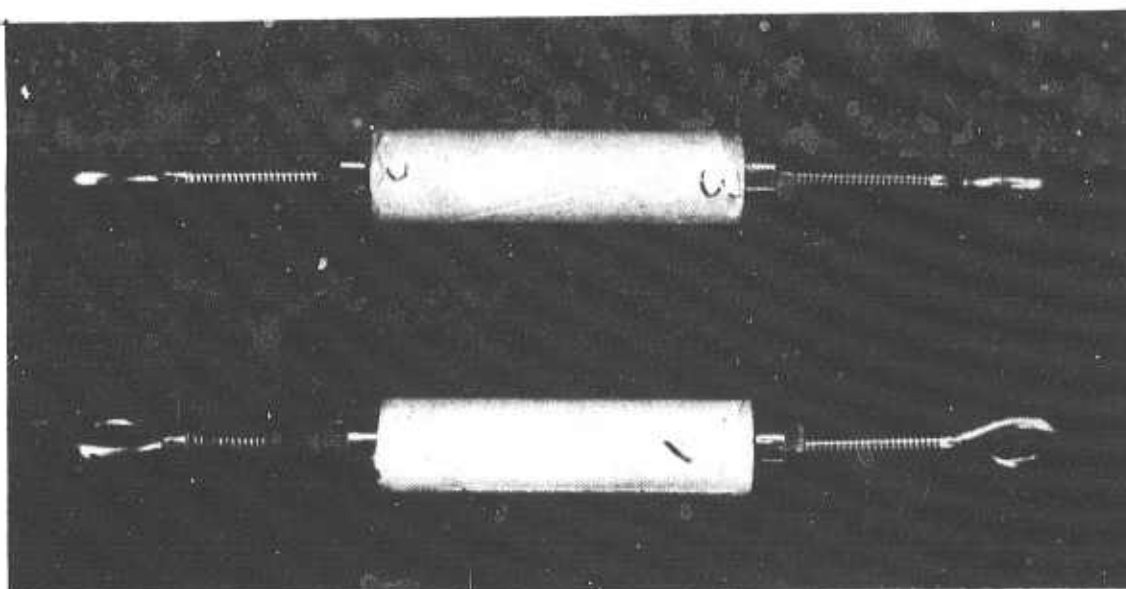
Static tensile and compressive tests were run on the principal material types with test data reported in Table 6. The tensile test specimens used had a nominal diameter of 0.75 in. by 3 in. long. Steel disks 0.25 in. thick were epoxied to the top and bottom surfaces of the specimen and eye bolts inserted into the disks for attachment to the loading machine as shown in Figure 23a. For the compression specimens, nominally 0.75 in. diameter were 0.5 in. long Teflon® sheets were used at the loading surfaces to minimize friction effects.

TABLE 5. SPECIMEN COMPOSITION

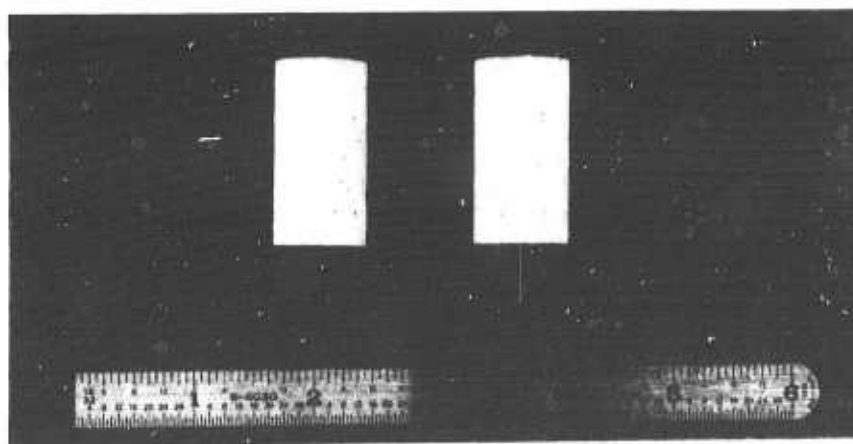
| Group No. | Aggregate | | | Mix Proportions | | Cure Time Days | Nominal Dia. in | Length in | Density lb/in ³ |
|--------------|-----------|-------|------|-----------------|---------------------|----------------------|-----------------------|--------------|-------------------------------|
| | No. | D50 | Cu | Water Cement | Aggregate Cement | | | | |
| 1 | | | | | | 7 | 0.75 | 18.0 | 0.0751 |
| 2 | A-3 | 0.425 | 1.64 | 0.56 | 2.0 | 7 | 1.50 | 18.0 | 0.0751 |
| 3 | | | | | | 28 | 0.75 | 18.0 | 0.0751 |
| 4 | A-4 | 1.30 | 1.49 | 0.50 | 2.0 | 7 | 1.50 | 18.0 | 0.0751 |

TABLE 6. AVERAGE STATIC PROPERTIES

| Group | Diameter in | Length in | Cure Time | Aggregate No. | Compression | | Tension | |
|-------|----------------|------------------|--------------|------------------|-----------------|-----------------------------------|-----------------|-----------------------------------|
| | | | | | Strength psi | Modulus psi x 10 ⁻⁶ | Strength psi | Modulus psi x 10 ⁻⁶ |
| 1 | 0.75 | 1.50-C 3.00-T | 7 | A-3 | 5990 | 2.80 | 352 | 3.61 |
| 2 | 1.50 | 3.00-C 6.00-T | 7 | A-3 | 5454 | 2.94 | 289 | 3.84 |
| 3 | 0.75 | 1.50-C 3.00-T | 28 | A-3 | 8184 | 5.51 | 358 | 5.49 |
| 4 | 1.50 | 3.00-C 6.00-T | 7 | A-4 | 5526 | 3.01 | 338 | 3.92 |



a) Tensile Specimens



b) Compression Specimens

Figure 23. Typical Specimens for Static Tests

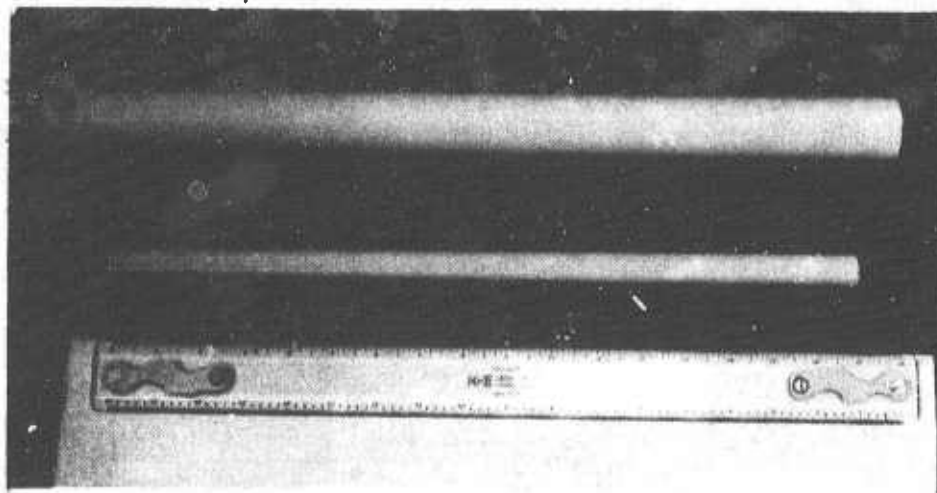


Figure 24. Dynamic Impact Bar Specimens

The tensile fracture studies were performed using an air gun assembly described in Reference 78 and shown in Figure 25. Some typical dynamically fractured tensile specimens are shown in Figure 26, and typical strain profiles for impacted concrete bars are shown in Figure 27. For the present tests, 1.0 in. and 2.0 in. long cylindrical steel impactors 0.485 in. in diameter with hemispherical noses were fired at capped and uncapped concrete bars with varying velocities so as to bracket the threshold tensile fracture stress.

The approximate values of the threshold fracture stresses were estimated by the following procedure. After the tests had been made on uninstrumented bars of various sizes with different aggregate sizes, several strain-gage instrumented bars were tested. The dynamic elastic modulus $E = \rho C^2$ was determined from measurements of wave speed C and the known density ρ . The instrumented bars were impacted first at very low velocities to measure wave speeds and then to higher velocities approaching the previously determined threshold impact velocity for tensile fracture. From the maximum strain recorded at the gage nearest the first observed fracture location the incipient fracture strain was estimated. The stress was then calculated by Hooke's Law with this strain and the previously determined dynamic modulus. The incipient tensile fracture stresses estimated by this procedure were on the order of 1.3 to 1.5 times the static tensile strengths given in Table 6. This is smaller than the factor of two customarily assumed⁽⁷³⁾ to relate the dynamic tensile strength of reinforced concrete to the static ultimate tensile strength.

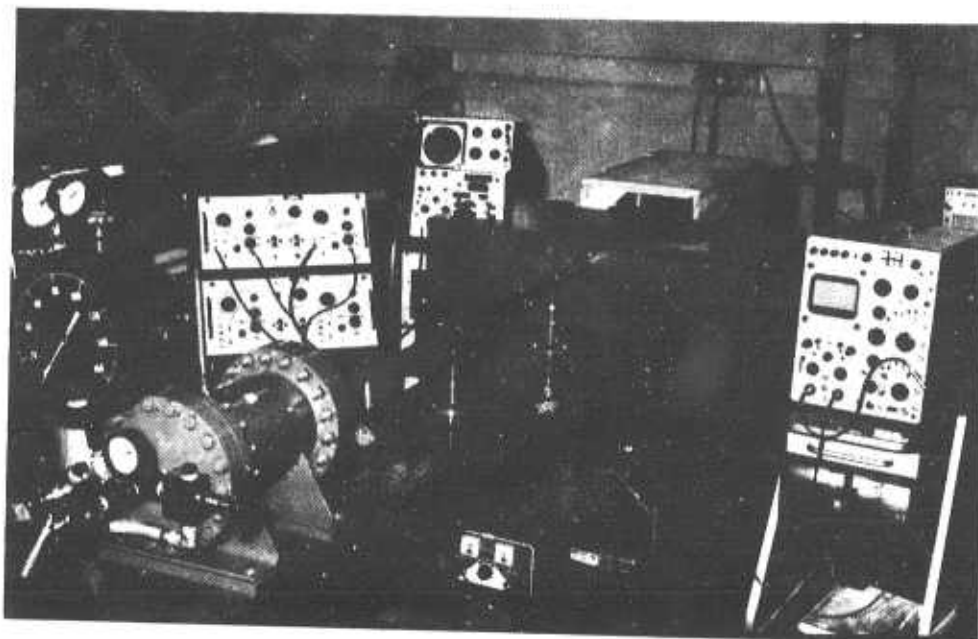


Figure 25. Dynamic Impact Test Assembly

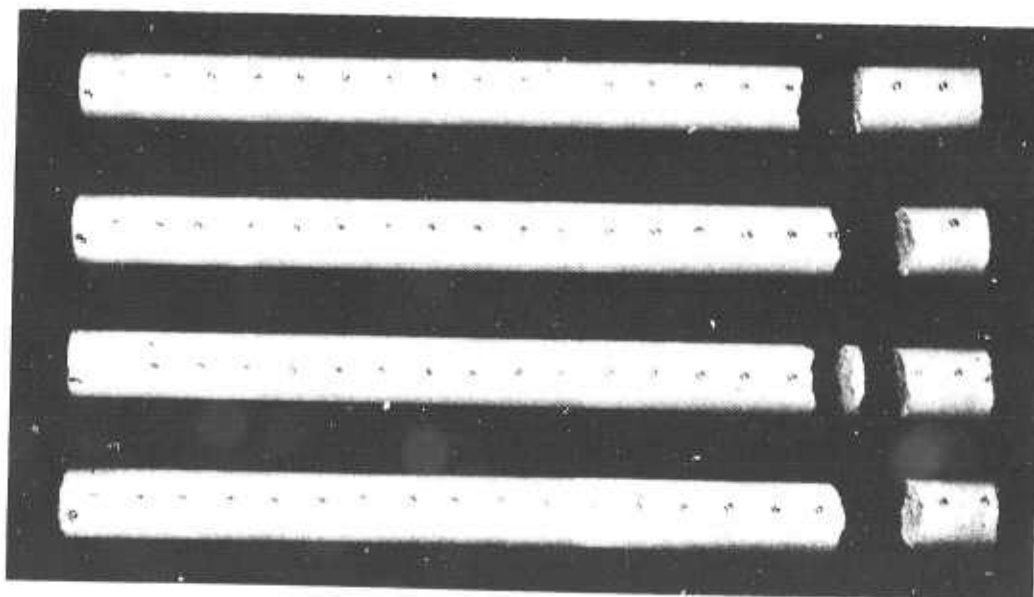
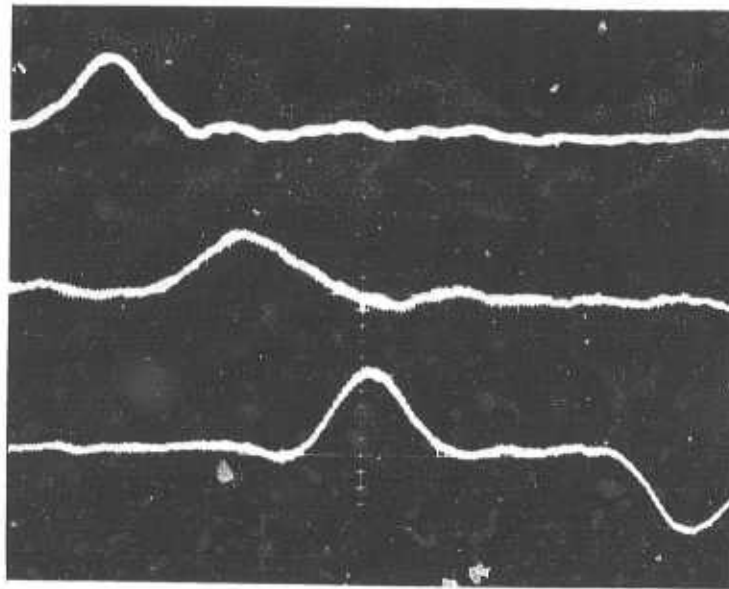
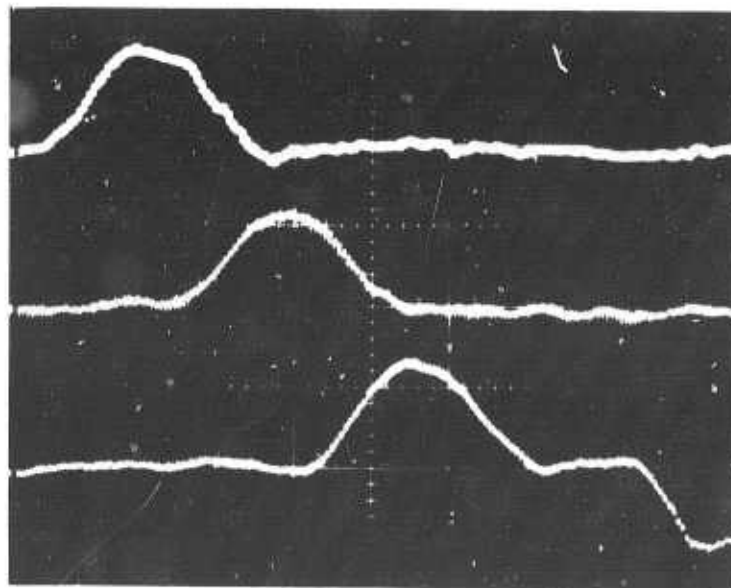


Figure 26. Typical Dynamic Tensile Fractures



a) Strain pulse propagating in a 1.50 inch diameter concrete bar, Bar 9, 1", 195 in/sec, C, A-3, 7, 20 μ sec/cm, 0.5 m volt/cm



b) Strain pulse propagating in a 1.50 inch diameter concrete bar, Bar 9, 2", 167 in/sec, C, A-3, 7, 20 μ sec/cm, 0.5m volt/cm

Figure 27. Typical Strain Profiles for Impacted Concrete Bars

The bars tested were of two different diameters and, in the case of the 1.5 in. diameter bars, of different aggregate composition. Since the input velocity required to produce tensile fracture was initially unknown, a range of impact velocities were used to establish the threshold limit. In some cases where the rod was not fractured, repeated tests were performed at the same or higher impact velocities to ascertain fracture initiation characteristics. Also, for some bars, the fracture zones were rebonded using a Devcon® "5-minute" epoxy and the specimens impacted at various velocities. Table 7 summarizes the results obtained for the tensile fracture stress studies. In Table 7, for non-fractured specimens, repeated impact studies were conducted to locate incipient fracture. These specimens have been denoted by a prime in the column of bar numbers. Repeated impact tests are useful in determining if the dynamic fracture characteristics have been changed by the passage of a non-destructive tensile wave through the specimen.

The experimental laboratory studies on tensile fracture in axially impacted concrete bars conducted at the University of Florida (Section 3.4) indicate that:

- (1) With longer impactors, tensile fractures tend to occur farther from the reflecting (free) end of the bar.
- (2) Tensile fracture locations in capped bars were reproducible. Those in uncapped bars were less consistent.
- (3) Uncapped bar specimens tend to give fractures farther from the free end than capped specimens.
- (4) Repeated impact tests on specimens that were re-glued after fracture tend to produce fractures at random positions.
- (5) Fracture locations occurring for comparable impact velocities in specimens of aggregate sizes A-3 and A-4 were similar as measured from the free end of the bar.
- (6) For the controlled aggregate sizes studied in this test series, scaling, as related to the tensile fracture locations for the bar geometries tested, was found to be relatively unimportant.
- (7) The dynamic threshold stress for incipient tensile fracture was estimated to be approximately 1.3 to 1.5 times the static ultimate tensile strength.

TABLE 7. DYNAMIC TENSILE FRACTURE
Type A-3 Concrete
0.75 in diameter by 18 in long

| Bar No. | Impact Velocity (in/sec) | Projectile Length (in) | Capped- Uncapped | Fracture Locations* (in) | Cure Cycle (days) |
|--------------------------------|-----------------------------|---------------------------|---------------------|-----------------------------|----------------------|
| 1 | 200 | 1.0 | C | 1.50 | 7 |
| 2 | 111 | 1.0 | C | No fracture | 7 |
| 3 | 150 | 1.0 | C | 2.385 | 7 |
| 4 | 123 | 1.0 | C | No fracture | 7 |
| 4' | 140 | 1.0 | C | 3.25 | 7 |
| 5 | 195 | 1.0 | U | No fracture | 7 |
| 6 | 258 | 1.0 | U | 3.13 | 7 |
| 7 | 221 | 1.0 | U | 3.63 | 7 |
| 8 | 216 | 1.0 | U | 4.25 | 7 |
| 9 | 256 | 1.0 | C | 2.25 | 28 |
| 10 | 185 | 1.0 | C | No fracture | 28 |
| 10' | 235 | 1.0 | C' | 1.63 | 28 |
| 11 | 213 | 1.0 | U | No fracture | 28 |
| 11' | 282 | 1.0 | U | 1.0, 3.25 | 28 |
| 12 | 290 | 1.0 | U | 1.0, 10.50 | 28 |
| Type A-3 Concrete | | | | | |
| 1.50 in diameter by 18 in long | | | | | |
| 1 | 1150 | 1.0 | C | 2.13, 2.75 | 7 |
| 2 | 1160 | 1.0 | C | 1.88 | 7 |
| 3 | 987 | 1.0 | C | 1.88, 2.13 | 7 |
| 4 | 769 | 1.0 | C | 1.88 | 7 |
| 5 | 500 | 1.0 | C | No fracture | 7 |
| 5' | 606 | 1.0 | C | 1.75, 4.00 | 7 |
| 6 | 769 | 1.0 | U | No fracture | 7 |
| 7 | 889 | 1.0 | U | No fracture | 7 |
| 8 | 909 | 1.0 | U | No fracture | 7 |
| 9 | 1000 | 1.0 | U | No fracture | 7 |
| 10 | 1230 | 1.0 | U | 1.0, 6.50 | 7 |
| Type A-4 Concrete | | | | | |
| 1.50 in diameter by 18 in long | | | | | |
| 1 | 769 | 2.54 | U | No fracture | 7 |
| 2 | 800 | 2.54 | U | 3.75 | 7 |

*Measured from free end of bar.

3.4 Conclusion

Not enough actual data on cratering in concrete was found to permit the deduction of any specific formulas or graphs for concrete similar to those presented in Section 3.2 for certain rock media. Because of the similarities between the material properties of concrete and of some of the rock media, it is believed that the same methods that have been successful in rock media could also be used for concrete if enough experimental data can be obtained under controlled conditions.

Empirical scaling methods similar to those represented in Figures 15 to 17 for spherical charge true surface shots (i.e., half buried) or near surface shots, with charges in intimate contact with the concrete, could certainly be applied. Because controlled tests on concrete would have fewer random variations in the medium than those in geologic materials, the modeling should be even better in the lower part of the charge weight range than the very good agreement shown by the Mine Shaft calibration series of Figures 15 to 17.

Small scale tests with charge weights varying over a range of the order of one pound to 27 pounds could be used to determine parameters in such empirical models. The one-pound charges in cement grout, reported in Table 4 of Section 3.2, were placed on cubical target blocks one yard on a side.

The largest crater formed had a radius about one-fourth of the block width and a depth about a third of the radius. This suggests that blocks of smaller depth than width could be used in the program if they were set in a dense soil or rock bed to minimize backface reflection and scabbing. This should be verified by comparison shots with the smaller charges. Geometric scaling would require a block three yards on a side for the 27-pound charges. A follow-up program should test the empirical formulas determined by the small-scale tests with a limited number of larger charges.

Effects of charge shape and contact conditions would also have to be studied. It was recognized at the beginning of Section 3.2 that successful empirical representation of controlled-condition surface-burst loadings, will, however, be of limited value for practical prediction of bomb damage after partial penetration. The importance of the contact conditions and the depth of burst cannot be overemphasized. Reinforcement and finite target thickness will also be important.

More advanced methods using numerical computation of a complete event (including penetration by a shaped charge followed by explosive cratering, spall and corner fractures) are certainly possible. But the development of constitutive models for use in such computations is still in the fundamental research phase. This fundamental research has made promising advances in other materials, including geologic materials with some similarities to concrete, but very little effort has been funded for concrete.

Much more fundamental research, especially experimental and theoretical work on material characterization (Section 3.3), is needed before a specific series of computer simulations of typical cases to obtain sets of tables and graphs for practical damage estimation can be prescribed. Such useful design aids can and should be developed when material characterizations sufficiently good to use in the computer simulations are available.

Two experimental lines of investigation are recommended to obtain dynamic material properties for these more fundamental approaches. These are uniaxial plane strain studies by plate-slap impact loading, and spherical wave studies similar to those described in Section 3.3-2 using multiple in-material gage records. With these experimental records available, one of the advanced constitutive models discussed in Section 3.3-3 could be fitted to the spherical wave data (for example, a capped elastic-plastic model) by using the Lagrangian analysis method of Section 3.3-4. After successful modeling of the spherical cavity expansion problems, the more difficult axisymmetric penetration and cratering problems could be attempted.

APPENDIX

LITERATURE SEARCH, LABORATORY VISITS, TECHNICAL MEETINGS

In conjunction with the specific areas of investigation noted in the introductory remarks, several literature search strategies and research information sources were used for pertinent unclassified subject references. The table below identifies the source agency and search title used for this purpose.

TABLE A-1. LIST OF LITERATURE SEARCHES

| Agency | Search Title |
|---|---|
| North Carolina Science and Technology Research Center | Effects of Pressure Blast Loading in Brittle Structural Materials |
| North Carolina Science and Technology Research Center | Dynamic Behavior of Concrete |
| Defense Documentation Center - Literature Survey | Blast Response of Concrete and Brittle Materials |
| Defense Documentation Center - Work Unit Summary Current Programs | Dynamic Behavior of Concrete |
| Smithsonian Science Information Exchange, Inc. | Dynamic Properties of Concrete |

In addition to the above literature searches, trips to active centers of research dealing with material removal and tensile fracture of concrete have been made. Also, several pertinent conferences dealing with dynamic effects in concrete, rock, and soil media have been attended and contacts with active investigators in these areas pursued.

A summary of places visited and pertinent meetings attended is included below.

TABLE A-2. PLACES AND LABORATORIES VISITED
AND CONFERENCES ATTENDED

| Research Laboratories | Conferences |
|---|---|
| Waterways Experiment Station | Accoustical Society of America Meeting, 29 Oct-2 Nov, 1973 (Wave Propagation Section) |
| Lawrence Livermore Lab | Mechanisms of Explosion and Blast Waves, 12-16 Nov, 1973 |
| U. S. Army Corps of Engineers (Livermore) | American Society of Mechanical Engineers, 11-15 Nov, 1973 (Rock mechanics) |
| Stanford Research Institute | Shock and Vibration Symposium 3-7 Dec, 1973 (Impact and Shock loading section) |
| Physics International | Seventh U.S. National Congress of Applied Mechanics, 3-9 June 1974 |

The computer searches produced little information directly applicable to the cratering/material removal problem. They did produce abstracts of papers in related areas as listed below in three categories.

TABLE A-3. CATEGORIES OF ABSTRACTS FROM LITERATURE SEARCH

| Area | Number of Abstracts |
|---------------------|---------------------|
| Blast Loading | 65 |
| Fracture | 23 |
| Material Properties | 15 |

Many of the abstracts in the blast loading category pertained to response characterization of concrete structural configurations such as arches, frames, slabs, and beam elements, while those categorized under fracture were associated with the topic of brittle fracture of materials, including concrete. The abstracts listed under material properties were concerned mainly with uniaxial and multiaxial testing, including the effects on material strength of such variables as aging, aggregate particle size, and water-cement ratio.

References cited in the text are listed in the following subsection. Most of these were not located by the computer searches, but were suggested by personal contacts with active investigators or discovered by scanning library copies of certain journals.

REFERENCES

1. Cristescu, N., Dynamic Plasticity, North-Holland Publishing Co., Amsterdam, 1967.
2. Johnson, N., Impact Strength of Materials, Edward Arnold, London, 1972.
3. Abrahamson, R. G., Florence, A. L., and Lindberg, H. E., "Radiation Damage Studies, Vol. XIII - Dynamic Response of Beams, Plates and Shells to Pulse Loads." BSD TR-66-372, Sept. 1966. UNCLASSIFIED.
4. Kay, F. J., and Whitehouse, G. D., "The Plastic Deformation of Clamped Rectangular Membranes Subjected to Impulsive Type Loading." Proceedings of the IASS Symposium, Hawaii, 1971. UNCLASSIFIED.
5. Huffington, N. J., Jr., "Blast Response of Panels," BRL TN 1702, August 1972. UNCLASSIFIED.
6. Ross, C. A., and Strickland, W. S., "Response of Flat Plates to Fuel Air Explosive (FAE) Loading Functions - A Membrane Analogy." Proceedings of Conference on Mechanism of Explosions and Blast Waves, Yorktown, Va. November 1973. UNCLASSIFIED.
7. Duwez, P. E., Clark, D. S., and Bohnenblust, H. F., "The Behavior of Long Beams Under Impact Loading." J. Appl. Mech. 72, 27 (1950). UNCLASSIFIED.
8. Lee, E. H., and Symonds, P. S., "Large Plastic Deformation of Beams under Transverse Impact." J. Appl. Mech., 74, 308 (1952).
9. Timoshenko, S. P., and Gere, J. M., Mechanics of Materials, Van Nostrand Reinhold Co., New York, N. Y., 1972, p. 288.
10. Symonds, P. S., Brown University Report UERD-3, 1955. UNCLASSIFIED.
11. Symonds, P. S., and Mentel, T. J., "Impulsive Loading of Plastic Beams with Axial Constraint," J. Mech. and Phys. of Solids, Vol. 6, 1958.
12. Symonds, P. S., and Jones, N., "Impulsive Loading of Fully Clamped Beams with Finite Plastic Deflections and Strain Rate Sensitivity," Int. J. of Mech. Sci. 14, 1972.

13. Menkes, S. B., and Opat, H. J., "Broken Beams," Experimental Mechanics, Vol. 13, No. 11, Nov. 1973.
14. Sewell, R. G. S., and Kinney, F. G., "Response of Structures to Blast: A New Criterion," Naval Weapons Center Report No. 4422, June 1968. UNCLASSIFIED.
15. Rinehart, J. S., and Pearson, J., Behavior of Metals Under Impulsive Loads, Dover Publ. Co., New York, N. Y., 1965.
16. "Effects of Impact and Explosion," AD 221586 Summary Technical Report of Div. 2 NDRC, Vol. 1, 1946. UNCLASSIFIED.
17. Lewis, B., and Von Elbe, G., Combustion, Flames and Explosions of Gases, Academic Press, Inc., New York, N. Y., 1951.
18. Stanyukovich, K. P., Unsteady Motion of Continuous Media, Translated by Holt, M., Pergamon Press, New York, N. Y., 1960.
19. Ross, C. A., and Strickland, W. S., "Response of Flat Plate Subjected to Mild Impulsive Loadings," 45th Shock and Vibration Symposium, Dayton, Ohio, 1974. UNCLASSIFIED.
20. Sichel, M., and Hu, C., "The Impulse Generated by Blast Waves Propagating Through Combustible Mixtures," Proceedings on Conference on Mechanism of Explosions and Blast Waves, Yorktown, Va., November 1973. UNCLASSIFIED.
21. Nicholls, J. A., et al., "Fundamental Aspects of Unconfined Explosions," US Air Force Technical Report, AFATL-TR-72-39, AF Armament Lab., Eglin AFB, Florida. March 1972. UNCLASSIFIED.
22. Nicholls, J. A., et al., "Fundamental Aspects of Unconfined Explosions," US Air Force Technical Report, AFATL-TR-73-125, AF Armament Lab., Eglin AFB, Florida. June 1973. UNCLASSIFIED.
23. Griner, G. R., "Dynamic Properties of Concrete," Master's Thesis, University of Florida, Engineering Sciences Department, Gainesville, Florida, 1974.
24. Davis, L. K., "Mine Shaft Series Events Mine Under and Mine Ore, Subtask N121, Crater Investigations," TR N-70-8, U. S. Army Engineers Waterways Experiment Station, Vicksburg, Mississippi, March 1970. UNCLASSIFIED.

25. Broberg, K. B., "Effect of Contact Detonation on Granite Slabs," Kungl. Fortifikationsforvaltningen Forskningssektionen, Report No. 109:15, Stockholm, Sweden, August 1960.
26. Effects of Impact and Explosion, NDRC Summary Report, 1946 (AD 221 586). UNCLASSIFIED.
27. Kaplan, K., "Experimental Study of the Effect of Material Properties on Coupling of Explosion Energy," AFSWC-TDR-63-47, Kirtland AFB, New Mexico, May 1963. UNCLASSIFIED.
28. Murphey, B. F., and Vortman, L. J., "High-Explosive Craters in Desert Alluvium, Tuff, and Basalt," J. of Geophysical Research, Vol. 66, pp. 3389-3404, 1961.
29. Nordyke, M. D., "Nuclear Craters and Preliminary Theory of the Mechanics of Explosive Crater Formation," J. of Geophysical Research, Vol. 66, pp. 3439-3459, 1961.
30. Vaile, R. B., Jr., "Pacific Craters and Scaling Laws," J. of Geophysical Research, Vol. 66, pp. 3413-3438, 1961.
31. Violet, C. E., "A Generalized Empirical Analysis of Cratering," J. of Geophysical Research, Vol. 66, pp. 3461-3470, 1961.
32. Cherry, J. T., "Computer Calculations of Explosion-Produced Craters," Int. J. Rock Mech. Min. Sci., Vol. 4, pp. 1-22 1967.
33. Rooke, A. D., Jr., Carnes, B. L., and Davis, L. K., "Cratering by Explosions: A Compendium and an Analysis," TR N-74-1, U. S. Army Waterways Experiment Station, Vicksburg, Mississippi, January 1974. UNCLASSIFIED.
34. Saxe, H. C., "Explosion Crater Prediction Utilizing Characteristic Parameters," pp. 273-305, in Rock Mechanics, Proc. 5th Symp. on Rock Mechanics, ed. C., Fairhurst, Oxford: Pergamon Press, 1963.
35. Teller, E., et al., The Constructive Uses of Nuclear Explosives, New York: McGraw-Hill, 1968.
36. Johnson, S. M., et al., Explosion Excavation Technology, NCG TR No. 21, U. S. Army Engineer Nuclear Cratering Group, Livermore, California, June 1971 (AD 727651). UNCLASSIFIED.

37. Johnson, J. B., "Feasibility of Model Studies in Blasting Research," pp. 267-271, Rock Mechanics, Proc. 5th Symp. on Rock Mechanics, ed. C. Fairhurst, Oxford: Pergamon Press, 1963.
38. D'Andrea, D. V., et al., "Crater Scaling in Granite for Small Charges," RI 7409, U. S. Bureau of Mines, 1970.
39. Haas, C. J., and Rinehart, J. S., "Coupling Between Unconfined Cylindrical Explosive Charges and Rock," Int. J. Rock Mech. Mining Sci., Vol. 2, pp. 13-24, 1965.
40. Vortman, L. J., "Craters from Surface Explosions and Scaling Laws," J. of Geophysical Research, Vol. 73, pp. 4621-4636, 1968.
41. Davis, L. K., "Mine Shaft Series, Subtask N123, Calibration Cratering Series," TR N-70-4, U. S. Army Waterways Experiment Station, Vicksburg, Mississippi, February 1970.
42. Rooke, A. D., Jr., and Davis, L. K., "Ferris Wheel Series, Flat Top Event, Project 1.9, Crater Measurements," POR-3008, August 1966, Atomic Energy Commission, Report prepared by U. S. Army Engineers Waterways Experiment Station, Vicksburg, Mississippi, and also published as its miscellaneous Paper No. 1-896. UNCLASSIFIED.
43. O'Brien, T. E., et al., "Multiple Threat Cratering Experiment, Vol. 1, Successive Cratering in Hard Rock" AFWL-TR-67-8, Kirtland AFB, New Mexico, April 1967. UNCLASSIFIED.
44. Read, H. E., and Maiden, C. J., "The Dynamic Behavior of Concrete," 3 SR-707, Systems, Science and Software, La Jolla, California, August 1971.
45. Butkovich, T. R., and Lewis, A. E., "Aids for Estimating Effects of Underground Explosions," UCRL-50929 Rev. 1, Lawrence Livermore Laboratory, Livermore, California, February 23, 1973.
46. Chou, P. C., and Hopkins, A. K., eds., Dynamic Response of Materials to Intense Impulsive Loads, Air Force Materials Laboratory, Metals and Ceramics Division, Wright-Patterson AFB, Ohio, 1973.
47. Wilkins, M. L., "Calculation of Elastic-Plastic Flow," pp. 211-263 in Methods in Computational Physics, Vol. 3, ed. B. Alder, New York: Academic Press, 1964.

48. Bertholf, L. D., and Benzley, S. E., "TOODY II, A Computer Program for Two-Dimensional Wave Propagation," Report SC-RR-68-41, Sandia Laboratories, Albuquerque, New Mexico, November 1968.
49. Maenchen, G., and Sack, S., "The Tensor Code," pp. 181-210 in Methods of Computational Physics, Vol. 3, ed. B. Adler et al., New York: Academic Press, 1964.
50. Read, H. E., and Maiden, C. J., "The Dynamic Behavior of Concrete," Topical Report 3 SR-707, Systems, Science and Software, La Jolla, California, August 1971.
51. Gregson, V. G., Jr., "A Shock Wave Study of Fondu-Fyre WA-1 and a Concrete," General Motors Materials and Structures Laboratory, Report MSL-70-30, 1971.
52. Swift, R. P., "Penetration Modeling of Concrete, A Research Suggestion," RS-5172-2, Physics International Co., San Leandro, California, November 1972.
53. Swift, R. P., "The Dynamic Response of Westerly Granite to Spherical Stress Waves," PIFR-146-3, Physics International Co., San Leandro, California, August 1971.
54. Swift, R. P., "Examination of the Static and Dynamic Material Response for a Mixed Company Sandstone," PITR-482, Physics International Co., San Leandro, California, November 1973.
55. Grady, D. E., Smith, C. W., and Seaman, L., "In Situ Constitutive Relations of Rocks," Final Report DNA-3172Z, Stanford Research Institute, Menlo Park, California, January 1973.
56. Danke, W. L., Jr., Schooley, D. J., and Jerozal, F. A., "Particle Velocimeter for Use Close-in to Underground Explosions," Final Report DASA 1431-3, Engineering Physics Co., Rockville, Maryland, October 1967.
57. Prater, R. F., "Hypervelocity Impact -- Material Strength Effects on Crater Formation and Shock Propagation in Three Aluminum Alloys," AFML TR 70-295, Wright-Patterson AFB, Ohio, December 1970. UNCLASSIFIED.
58. Kinslow, R., ed., High-Velocity Impact Phenomena, New York: Academic Press, 1970.
59. Burke, J. J., and Weiss, V. eds., Shock Waves and the Mechanical Properties of Solids, Syracuse: Syracuse University Press, 1971.

60. Bekey, G. A., "Systems Identification -- An Introduction and a Survey," Simulation, Vol. 15, 151-166, 1970.
61. Fowles, G. R., and Williams, R. F., "Plane Stress Wave Propagation in Solids," J. Appl. Phys., Vol. 41, 360-363, 1970.
62. Cowperthwaite, M., and Williams, R. F., "Determination of Constitutive Relations with Multiple Gages in Non-divergent Waves," J. Appl. Phys., Vol. 42, 456-462, 1971.
63. Fowles, R., "Conservation Relations for Spherical and Cylindrical Stress Waves," J. Appl. Phys., Vol. 41, 2740-2741, 1970.
64. Nelson, I., Baron, M. L., and Sandler, I., "Mathematical Models for Geological Materials for Wave-Propagation Studies," pp. 289-351 in Reference 59.
65. Green, S. J., et al., "Constitutive Relations for Concrete at Intermediate Pressure Levels," Report AFWL-TR-71-34, Terra Tek, Inc., Salt Lake City, Utah, 1971. UNCLASSIFIED.
66. Seaman, L., Barbee, T. W., and Curran, D. R., "Dynamic Fracture Criteria of Homogeneous Materials," AFWL-TR-71-156, Stanford Research Institute, Menlo Park, California, December 1971. UNCLASSIFIED.
67. Barbee, T., Seaman, L., and Crowdson, R. C., "Dynamic Fracture Criteria of Homogeneous Materials," AFWL-TR-70-99, Stanford Research Institute, Menlo Park, California, November 1970. UNCLASSIFIED.
68. Shockey, D. A., Curran, D. R., DeCarli, P. S., Wilhelm, J. P., and Petro, D., Final Report - Phase II for U. S. Army BRL, Contract DAAD05-73-C-0025, SRI Project PYU-2151, Stanford Research Institute, Menlo Park, California, March 1974.
69. Shockey, D. A., Seaman, L., and Curran, D. R., "Dynamic Fracture of Beryllium Under Plate Impact and Correlation with Electron Beam and Underground Test Results," Final Report AFWL-TR-73-12, Stanford Research Institute, Menlo Park, California, January 1973. UNCLASSIFIED.
70. Shockey, D. A., Petersen, C. F., Curran, D. R., and Rosenberg, J. T., "Dynamic Tensile Fracture in Rocks," for Bureau of Mines, Annual Technical Report, by Stanford Research Institute, Menlo Park, California, March 1972.

71. Shockey, D. A., Curran, D. R., Seaman, L., Rosenberg, J. T., and Petersen, C. F., "Fragmentation of Rock Under Dynamic Loads," to be published in Int. J. of Rock Mech. and Min. Sci.
72. Petersen, C. F., and Erlich, D. C., "Dynamic Properties of Rock Required for Prediction Calculations," DNA-3123F for Defense Nuclear Agency, by Stanford Research Institute, Menlo Park, California, November 1972.
73. Birkimer, D. L., and Lindemann, R., "Dynamic Strength of Concrete Materials," Journal of the American Concrete Institute, V. 68, pp. 47-49, 1971.
74. Watstein, D., "Effect of Straining Rate on the Compressive Strength and Elastic Properties of Concrete," Journal of the American Concrete Institute, Vol. 50, pp. 729-744, 1953.
75. Goldsmith, W., Polivka, M., and Young, T., "Dynamic Behavior of Concrete," Experimental Mechanics, Vol. 6, pp. 65-79, 1966.
76. Goldsmith, W., Kenner, V. H., and Ricketts, T. E., "Dynamic Loading of Several Concrete-Like Mixtures," Proceedings of the American Society of Civil Engineers-Structural Division, Vol. 94, pp. 1803-1827, 1968.
77. Oh, K. P. L., and Finnie, I., "On the Location of Fracture in Brittle Solids Due to Wave Propagation in a Slender Rod," International Journal of Fracture Mechanics, Vol. 6, pp. 333-339, 1970.
78. Nevill, G. E., Jr., Sierakowski, R. L., Ross, C. A., and Jones, E. R., "One-Dimensional Wave Pulses in Steel-Epoxy Composites," Experimental Mechanics, Vol. 3, pp. 278-282, 1972.

INITIAL DISTRIBUTION

| | |
|-------------------------------|---|
| AMXSY-A | 1 |
| AFML/LNP | 1 |
| AFIT/ENB | 1 |
| ASD/ENYS | 1 |
| ASD/ENYS/Armament Engr | 1 |
| NASA Msc Ctr | 1 |
| USNRL/Code 5180 | 1 |
| USNWL/Code MAL | 1 |
| USNWC/Code 4566 | 1 |
| USNWC/Code 456 | 1 |
| USNWC/Code 4544 | 1 |
| USNWC/Code 454 | 1 |
| AMXRD-BVL | 1 |
| AUL (AUL/LSE-70-239) | 1 |
| DDC | 2 |
| Redstone Sci Info Ctr/Doc Sec | 2 |
| AFATL/DLOSL | 2 |
| AFATL/DL | 1 |
| AFSC/DLSW | 1 |
| Explosives Safety Bld | 1 |
| ASD/TWT | 1 |
| US Army R&D Ctr/AMXRD-AD | 1 |
| Hq USAF/SAMI | 1 |
| TAWC/TRADOCLO | 1 |
| Hq 4950 TESTW/TZHM | 1 |
| Ogden ALC/MANOP | 2 |
| AFWL/LR | 2 |